

Asymmetric semi-infinite nuclear matter: surface and curvature properties in relativistic and non-relativistic models

M. Centelles, M. Del Estal, X. Viñas

*Departament d'Estructura i Constituents de la Matèria, Facultat de Física,
Universitat de Barcelona, Diagonal 647, E-08028 Barcelona, Spain*

Abstract

Surface and curvature properties of asymmetric semi-infinite nuclear matter are studied to beyond the proton drip. Using the semiclassical extended Thomas–Fermi method, the calculations are performed in the non-relativistic and relativistic mean field theories (Skyrme forces and non-linear σ – ω parametrizations). First we discuss the bulk equilibrium between the nuclear and drip phases. Next we analyze the asymmetric surface as a function of the bulk neutron excess. We examine local quantities related to the density profiles and, for two definitions of the bulk reference energy, the surface and curvature energy coefficients. The calculation of the curvature energy is carefully treated. The sensitivity of the nuclear surface to the relativistic effects is investigated. Mass formulae useful for arbitrary neutron excess are discussed, and their limit at small asymmetries is compared with the liquid droplet model mass formula.

PACS: 21.60.-n, 21.10.Dr, 21.65.+f

1 Introduction

In several problems of nuclear physics and astrophysics the surface and curvature properties of nuclei play a crucial role. This is the case, for instance, of barrier heights and saddle-point configurations in nuclear fission, or of fragment distributions in heavy-ion collisions. In astrophysical applications they are important for equilibrium sizes, electron capture rates and level densities used in describing neutron stars and supernovae. However, the proton fraction of the nuclei involved in these problems is rather different. For terrestrial nuclei the proton fraction is around 0.4–0.5, whereas the astrophysical problems demand a smaller proton concentration and, furthermore, to consider nuclei surrounded by an external gas of drip neutrons. Therefore, there is a strong motivation for studying the surface and curvature properties of nuclei in the whole range of asymmetries, between nuclear and neutron matter.

Within a context related to the liquid droplet model (LDM) and the leptodermous expansion of a finite nucleus [1], the surface and curvature energy coefficients can be extracted from semi-infinite nuclear matter. This schematic geometry avoids undesired shell, Coulomb and finite-size effects, which makes it very appropriate to study surface properties. Many of the calculations have been carried out using the semiclassical extended Thomas–Fermi (ETF) method [2,3,4] together with Skyrme forces [5]. For the case of symmetric semi-infinite matter, the reader can consult e.g. Refs. [4,6,7,8]. Although the surface energy can be calculated in a fully quantal way, only one part of the curvature energy can be obtained from a quantum-mechanical calculation [8,9]. This is an important reason to compute the surface and curvature coefficients by means of a semiclassical approach.

As far as asymmetric semi-infinite nuclear matter is concerned, we may point out two publications of particular relevance for the present work. The surface energy of multi-component systems up to the proton drip was investigated by Myers *et al.* [10] in the Thomas–Fermi (TF) approximation with the Seyler–Blanchard interaction. Almost at the same time, Kolehmainen *et al.* [11] performed an analysis of the surface and curvature effects of neutron-rich nuclei, including drip neutrons, with the ETF method and Skyrme forces.

In recent years the relativistic treatment of the nuclear many-body problem has been a

subject of growing interest [12,13,14,15]. The relativistic theory, already in the mean field (Hartree) approximation, automatically includes the spin-orbit force and the finite range and density dependence of the nuclear interaction. All these effects are very important for the surface properties of a nuclear system [16]. The phenomenological $\sigma-\omega$ model of Walecka and its extensions [12,17] have become very popular in relativistic nuclear calculations. They have been widely employed in the Hartree approach for describing ground-state properties of nuclei [18,19,20,21] as well as symmetric semi-infinite nuclear matter [17,22,23].

Until recently the semiclassical approach to the relativistic mean field theory had been settled at the TF level only [12,17,24,25,26]. However, in the last years some amount of work has been addressed to develop the relativistic extended Thomas–Fermi (RETF) method [27,28,29,30], that includes gradient corrections of order \hbar^2 in the particle density and the scalar field. This new semiclassical approach has already been applied to the study of finite nuclei [28,31,32,33] and of the nuclear surface in the symmetric case [28,34,35]. In comparison with quantal calculations, the inclusion of the gradient corrections to the TF method improves the surface properties (energy and profile) [31,34,35]. Moreover, the quality of the RETF results is less dependent on the parameters of the relativistic interaction than in the TF approximation.

The asymmetric matter has also been investigated within the relativistic theory. For example, the infinite system has been analyzed in the Dirac–Hartree–Fock approach [36], and surface properties at low proton concentrations have been computed with the TF method [37]. Müller and Dreizler [38] have calculated relativistic hot asymmetric nuclear matter and nuclei, and in Ref. [39] Müller and Serot have carefully dealt with the subject of phase transitions in asymmetric nuclear matter at finite temperature. Other works on relativistic asymmetric systems have been concerned, e.g., with neutron star properties [40] or collective modes and response functions [41].

The main aim of this paper is to analyze, from a semiclassical point of view, the surface and curvature properties of asymmetric semi-infinite nuclear matter in the non-relativistic and relativistic frameworks. For this purpose we will use the ETF and RETF methods respectively. Our study covers the range of proton concentrations from symmetric nuclear

matter to beyond the proton drip. We will put special emphasis on the calculation of the curvature energy, that can be fully obtained only within the semiclassical approach and in which some confusion exists [8,9,35].

The paper is organized as follows. Section 2 is devoted to the study of uniform asymmetric nuclear matter with arbitrary proton concentration, including drip neutrons and protons. In the third section we derive the equations for the interface surface and curvature properties in the general case with drip particles. Numerical investigations are presented and discussed in Section 4. The summary and conclusions are given in the last section.

2 The bulk equilibrium

Before proceeding to study the surface properties of nuclei in coexistence with drip nucleons, we start by the simpler model of two infinite pieces of asymmetric nuclear matter in equilibrium. The uniform phase with the higher density and a given proton concentration represents a nucleus that is in equilibrium with a surrounding gas of drip nucleons. The latter is represented by the lower density phase, with another proton concentration. This approach neglects the interface effects and reflects the situation of the equilibrium densities very far from the interface region in either direction.

The asymmetric nuclear matter problem including drip particles has a notable similitude with the problem of the coexistence between nuclei and evaporated nucleons at finite temperature [38,42,43,44]. Actually, the bulk equilibrium of asymmetric matter at finite temperature was investigated time ago within the astrophysical context [45,46], and more recently in Refs. [39,47]. In this section we perform a similar analysis at $T = 0$ based on the relativistic non-linear $\sigma-\omega$ model, with care over the effects of the proton concentration. However, our discussion is rather general and can be applied to the non-relativistic treatment of cold asymmetric nuclear matter as well.

First we consider an infinite system made up of two components (neutrons and protons) in a single phase. For describing asymmetric matter it is convenient to switch variables from the neutron and proton densities ρ_n and ρ_p to the total density ρ and the relative neutron excess δ :

$$\rho = \rho_n + \rho_p \quad (2.1)$$

$$\delta = \frac{\rho_n - \rho_p}{\rho}. \quad (2.2)$$

If we call $\mathcal{E}(\rho, \delta)$ the energy density of the system, then the neutron and proton chemical potentials and the pressure are

$$\mu_n = \frac{\partial \mathcal{E}(\rho, \delta)}{\partial \rho_n} = \frac{\partial \mathcal{E}}{\partial \rho} \frac{\partial \rho}{\partial \rho_n} + \frac{\partial \mathcal{E}}{\partial \delta} \frac{\partial \delta}{\partial \rho_n} = \frac{\partial \mathcal{E}}{\partial \rho} + \frac{\partial \mathcal{E}}{\partial \delta} \frac{1 - \delta}{\rho} \quad (2.3)$$

$$\mu_p = \frac{\partial \mathcal{E}(\rho, \delta)}{\partial \rho_p} = \frac{\partial \mathcal{E}}{\partial \rho} \frac{\partial \rho}{\partial \rho_p} + \frac{\partial \mathcal{E}}{\partial \delta} \frac{\partial \delta}{\partial \rho_p} = \frac{\partial \mathcal{E}}{\partial \rho} - \frac{\partial \mathcal{E}}{\partial \delta} \frac{1 + \delta}{\rho} \quad (2.4)$$

$$P = -\frac{\partial}{\partial(1/\rho)} \left[\frac{\mathcal{E}(\rho, \delta)}{\rho} \right] = \rho^2 \frac{\partial}{\partial \rho} \left[\frac{\mathcal{E}(\rho, \delta)}{\rho} \right] = \rho \frac{\partial \mathcal{E}}{\partial \rho} - \mathcal{E}. \quad (2.5)$$

Manipulating these expressions, one gets that the pressure is related with the neutron and proton chemical potentials through

$$P = \mu_n \rho_n + \mu_p \rho_p - \mathcal{E}(\rho, \delta). \quad (2.6)$$

At saturation $P = 0$ and the preceding equation is, actually, a generalization of the Hugenholtz–Van Hove theorem [48,49]. The incompressibility at saturation of asymmetric nuclear matter with relative neutron excess δ reads

$$K(\rho_{\text{sat}}, \delta) = 9\rho^2 \frac{d^2}{d\rho^2} \left(\frac{\mathcal{E}(\rho, \delta)}{\rho} \right) \Big|_{\rho_{\text{sat}}}, \quad (2.7)$$

where ρ_{sat} is the saturation density that conforms Eq. (2.6) with $P = 0$. The expression of the energy density \mathcal{E} for the relativistic model and for Skyrme forces can be found in Appendix A. There, \mathcal{E} is given including the semiclassical gradient corrections of order \hbar^2 which, of course, vanish in the uniform infinite geometry.

The asymmetric nuclear matter in a single phase is not stable at all densities and δ values. At zero temperature, the necessary and sufficient conditions for the stability of a binary system can be expressed through the inequalities [39,46,50]

$$K = \left(\frac{\partial P}{\partial \rho} \right)_\delta \geq 0 \quad (2.8)$$

$$\left(\frac{\partial \mu_n}{\partial \delta} \right)_P \geq 0 \quad \text{or} \quad \left(\frac{\partial \mu_p}{\partial \delta} \right)_P \leq 0. \quad (2.9)$$

In addition, the pressure P must be positive. A positive incompressibility K guarantees mechanical stability, and the condition on the derivatives of the chemical potential ensures diffusive stability. Violation of the stability criteria signals phase separation. The system ceases to exist as a phase alone and splits into separate phases in equilibrium. However, instability is only a sufficient condition and phase separation may take place when the single-phase system is stable (in general, metastable).

Now we address the problem of the coexistence of two phases in a two-component system. One of the phases represents an asymmetric uniform nuclear system with density ρ_0 and

relative neutron excess δ_0 . The other phase corresponds to a uniform phase of drip particles characterized by ρ_d and δ_d . Equation (2.6) is still valid for each separate phase, but at equilibrium the pressure is no longer zero. In the general case with drip neutrons and protons, the two phases can coexist when the following conditions are fulfilled:

$$\mu_{n0} = \mu_{nd} \quad (2.10)$$

$$\mu_{p0} = \mu_{pd} \quad (2.11)$$

$$P_0 = P_d, \quad (2.12)$$

which in view of Eq. (2.6) result in

$$\mu_n(\rho_{n0} - \rho_{nd}) + \mu_p(\rho_{p0} - \rho_{pd}) = \mathcal{E}_0 - \mathcal{E}_d. \quad (2.13)$$

Equations (2.10)–(2.12) allow one to get ρ_0 , ρ_d and δ_d for a fixed value of δ_0 in the nuclear phase. Notice that the solution of the above equations does not correspond to the saturation conditions at δ_0 and δ_d . As a consequence, the energy of the nuclear and drip phases in coexistence is not a minimum.

The numerical results of this section will be discussed for the NL1 parametrization of the relativistic non-linear $\sigma-\omega$ model [20]. Other $\sigma-\omega$ parameter sets or non-relativistic Skyrme forces qualitatively show the same trends. The saturation properties of NL1 are given in Table 1, together with those of other interactions we will utilize later in the calculation of surface properties.

To study the different regimes of phase coexistence, Fig. 1 displays the neutron and proton chemical potentials against the relative neutron excess for NL1. At small values of δ_0 there are no drip particles and the nuclear matter fulfills the usual saturation condition. In this first stage the chemical potentials are negative. While for neutrons the chemical potential is an increasing function of δ_0 , it decreases steadily for protons. The point where the neutron chemical potential vanishes marks the onset of the neutron drip. At this moment the coexistence between the nuclear and drip phases, the latter containing only neutrons ($\delta_d = 1$), starts to be possible. In this second regime, that for NL1 covers the range $0.24 \leq \delta_0 \leq 0.64$ approximately, the neutron chemical potential ($\mu_{n0} = \mu_{nd}$) is positive.

Since there are no protons in the drip matter yet, the proton chemical potentials μ_{p0} and μ_{pd} of the nuclear and drip phases are different. Both μ_{p0} and μ_{pd} are negative, being lowered by raising the neutron excess. Due to the fact that μ_{pd} is larger and decreases at a faster rate than μ_{p0} , they match at some large δ_0 , which for NL1 happens at $\delta_0 \simeq 0.64$. This is just the point where protons start to drip. The last two rows in Table 1 display the values of δ_0 at the neutron and proton drip points (labelled $\bar{\delta}_{nd}$ and $\bar{\delta}_{pd}$).

For larger δ_0 the drip phase contains a small proton concentration ($\delta_d < 1$). The two phases disappear when the solution of Eqs. (2.10)–(2.12) yields the same density and neutron excess in the nuclear and drip regions. This solution is just the critical point characterized by ρ_c and δ_c , see Eq. (2.14) below. It corresponds to the maximum of $\mu_{n0}(\delta)$ and to the minimum of $\mu_{p0}(\delta)$. For δ larger than δ_c the dashed lines in Fig. 1 represent the neutron and proton chemical potentials of the drip matter only. Tracing horizontal lines in the $\mu - \delta$ plane one can read, at the left and right hand sides of the critical value δ_c , the relative neutron excess of the nuclear and drip phases in coexistence beyond the proton drip point.

Figure 2 shows the nuclear and drip densities, ρ_0 and ρ_d , as a function of the square of the neutron excess for NL1. For small values of δ_0 the nuclear density ρ_0 has a linear behaviour with δ_0^2 , as expected from the droplet model [1]. The density of the nuclear (drip) phase falls (climbs) with increasing δ_0^2 . Both densities coincide at the critical δ_c . The dashed line of Fig. 2 represents the density of the drip region for $\delta^2 > \delta_c^2$. As in Fig. 1, by drawing horizontal lines it serves to read the equilibrium values of δ_0^2 and δ_d^2 when protons have migrated to the drip phase.

The equation of state of NL1 at several values of δ is displayed by solid lines in Fig. 3. The dot-dashed line defines the boundary of the coexistence region. The long-dashed and short-dashed lines are the diffusive and mechanical stability lines respectively. We have joined by dashed horizontal lines a few examples of points on the coexistence curve, belonging to the nuclear and drip phases, that can be in equilibrium. The common maximum of the coexistence and diffusive stability lines corresponds to the critical point (δ_c, ρ_c) determined by

$$\left(\frac{\partial\mu_n}{\partial\delta}\right)_P = \left(\frac{\partial^2\mu_n}{\partial\delta^2}\right)_P = 0. \quad (2.14)$$

The line of mechanical stability lies in the negative pressure region. Therefore, it does not play any role in the separation of the system in two phases, that is completely ruled by the diffusive instability. The zone between the coexistence and diffusive stability lines is the metastable region where the binary system may remain in a single phase or undergo phase separation.

Consider a uniform nuclear system with density ρ and neutron excess δ under a pressure P . If the representative point in the $P - \rho$ diagram of Fig. 3 lies outside the coexistence region, the system is in a single phase. If the system is expanded along a line of constant δ it will remain in a single phase up to crossing the coexistence line, where phase separation can occur. Denoting by ξ the mass fraction of the nuclear phase (δ_0, ρ_0) in coexistence with the incipient drip phase (δ_d, ρ_d) , with mass fraction $1 - \xi$, the following relationships are to be satisfied at that point:

$$\delta = \xi\delta_0 + (1 - \xi)\delta_d \quad (2.15)$$

$$\frac{1}{\rho} = \frac{\xi}{\rho_0} + \frac{1 - \xi}{\rho_d}. \quad (2.16)$$

In Figs. 4 and 5 we plot in the $\mu_n - \rho$ and $\mu_p - \rho$ planes the lines of coexistence (solid), diffusive stability (long dash) and mechanical stability (short dash) for NL1. The chemical potentials and densities at the right and left hand sides of the critical point (the maximum and the minimum of the coexistence line in the $\mu_n - \rho$ and $\mu_p - \rho$ planes) correspond to the nuclear and drip phases respectively. The dashed straight lines joining points of the coexistence curve indicate some possible values of the densities and chemical potentials in the phase equilibrium. Notice that in the $\mu_p - \rho$ plane some of these straight lines are not horizontal. In such cases the drip phase does not contain protons ($\delta_d = 1$) and the proton chemical potentials of both phases are different, see Fig. 1. When the proton drip point is reached these lines turn horizontal, indicating that $\mu_{p0} = \mu_{pd}$.

3 Surface properties in two-component systems

On the basis of asymmetric semi-infinite nuclear matter, in this section we shall study the surface effects of a neutron-rich nucleus immersed in a gas of drip particles. This regime corresponds to the physical situation found in neutron stars, at densities between 4×10^{11} g/cm³ and normal nuclear values (2.7×10^{14} g/cm³) [51]. First of all it is necessary to determine the density profile from which the surface and curvature energies can be obtained. To do that one considers a semi-infinite slab with a plane interface separating a mixture of protons and neutrons to the left and a gas of drip particles to the right. The axis perpendicular to the interface is taken to be the z axis. The density profile is sketched in Fig. 6. Observe that the relative neutron excess δ depends on the z coordinate. When z goes to minus infinity, the neutron and proton densities approach the values that in uniform nuclear matter are in equilibrium with a uniform gas of drip particles. Therefore, for a given bulk neutron excess $\delta_0 \equiv \delta(-\infty)$, the values of $\rho(-\infty)$, $\rho(\infty)$ and $\delta(\infty)$ are just the ρ_0 , ρ_d and δ_d solutions to Eqs. (2.10)–(2.12).

The problem of finding the density profile at a certain value of δ_0 when drip particles appear is, in a sense, formally equivalent to solving the problem of a warm nucleus. In that case, as it was pointed out by Bonche *et al.* [43], the Hartree–Fock equations at some temperature and chemical potential possess two different solutions. One of them represents the nuclear system in equilibrium with its evaporated nucleons. The other one belongs to the evaporated nucleon gas alone. It is then natural to define extensive magnitudes characterizing the nucleus as the *difference* between their value in the nuclear-plus-gas solution and their value in the gas solution. The same idea has been applied in the semiclassical scheme for the Euler–Lagrange equations at finite temperature [44].

To compute semiclassically the proton and neutron densities in asymmetric semi-infinite nuclear matter one has to minimize the total energy per unit area. This has to be done with the constraint of conservation of the number of neutrons and protons with respect to arbitrary variations of the densities. According to the above discussion, the energy, neutron and proton densities entering the constrained energy of the (semi-infinite) nucleus will be taken as the difference between the ones of the whole system (nucleus plus drip particles),

and those of the uniform gas of drip particles (indicated by a d subscript). For instance we will write the local energy density representing the nucleus, i.e. the subtracted system, in the form $\mathcal{E}(z) - \mathcal{E}_d$. As $z \rightarrow -\infty$ we have $\mathcal{E}(z) \rightarrow \mathcal{E}_0$, while as $z \rightarrow \infty$ it is $\mathcal{E}(z) \rightarrow \mathcal{E}_d$. Due to the absence of Coulomb forces in the semi-infinite problem, the drip particles are described by plane waves and behave as a dilute uniform phase.

Then, we write the constrained energy per unit area as

$$\frac{E_{\text{const}}}{S} = \int_{-\infty}^{\infty} dz \{ \mathcal{E}(z) - \mathcal{E}_d - \mu_n[\rho_n(z) - \rho_{nd}] - \mu_p[\rho_p(z) - \rho_{pd}] \}. \quad (3.1)$$

For the whole system, the proton and neutron densities are obtained from the following coupled Euler–Lagrange equations:

$$\frac{\delta \mathcal{E}(z)}{\delta \rho_n} - \mu_n = 0, \quad \frac{\delta \mathcal{E}(z)}{\delta \rho_p} - \mu_p = 0. \quad (3.2)$$

In the relativistic framework one has three additional equations, originating from the variations with respect to the fields ϕ , V and R associated with the σ , ω and ρ mesons:

$$\frac{\delta \mathcal{E}(z)}{\delta \phi} = 0, \quad \frac{\delta \mathcal{E}(z)}{\delta V} = 0, \quad \frac{\delta \mathcal{E}(z)}{\delta R} = 0. \quad (3.3)$$

We recall the reader that the ETF and RETF expressions for \mathcal{E} are detailed in Appendix A. The drip particles obey analogous equations:

$$\frac{\delta \mathcal{E}_d}{\delta \rho_{nd}} - \mu_n = 0, \quad \frac{\delta \mathcal{E}_d}{\delta \rho_{pd}} - \mu_p = 0, \quad (3.4)$$

plus in the relativistic case

$$\frac{\delta \mathcal{E}_d}{\delta \phi_d} = 0, \quad \frac{\delta \mathcal{E}_d}{\delta V_d} = 0, \quad \frac{\delta \mathcal{E}_d}{\delta R_d} = 0. \quad (3.5)$$

The local equations (3.2) and (3.3) are self-consistently solved by numerical iteration. As explained in Ref. [28], we employ the imaginary time-step method to get the densities from Eq. (3.2) and Gaussian elimination to get the meson fields from Eq. (3.3). Given δ_0 , the asymptotic boundary conditions to be imposed stem from the coexistence equations (2.10)–(2.12). Equations (3.4) and (3.5) are satisfied by the low-density phase solution of (2.10)–(2.12), which provides the limiting behaviour as $z \rightarrow \infty$. On the other hand, the high-density solution of (2.10)–(2.12) represents the system at $z = -\infty$.

Once the density profiles are known, the next step is to get the surface and curvature energy coefficients. The surface tension (i.e. the surface energy per unit area of a flat surface) may be written as [1,10,11]

$$\sigma = \int_{-\infty}^{\infty} dz [\mathcal{E}(z) - \mathcal{E}_d - \mathcal{E}_{\text{ref}}(z)], \quad (3.6)$$

where $\mathcal{E}_{\text{ref}}(z)$ is a reference energy density whose integral represents in some way the bulk contribution. Myers *et al.* [10] noted that there are two possibilities to define $\mathcal{E}_{\text{ref}}(z)$.

The first definition corresponds to a reference energy that represents the energy a nucleus would have if its nucleons would belong to infinite nuclear matter. This reference energy density is to be written as

$$\mathcal{E}_{\text{ref}}^e(z) = \frac{\mathcal{E}_0 - \mathcal{E}_d}{\rho_0 - \rho_d} [\rho(z) - \rho_d], \quad (3.7)$$

which we will call the e-definition following Ref. [10]. In this case the surface tension reads

$$\sigma_e = \int_{-\infty}^{\infty} dz \left\{ \mathcal{E}(z) - \mathcal{E}_d - \frac{\mathcal{E}_0 - \mathcal{E}_d}{\rho_0 - \rho_d} [\rho(z) - \rho_d] \right\}. \quad (3.8)$$

The second definition of the reference energy will be called the Gibbs definition. Instead of the bulk energy per particle, it introduces the neutron and proton chemical potentials and the pressure associated with the bulk. The Gibbs reference energy for the whole system is

$$E_{\text{ref}}^\mu = \mu_n N + \mu_p Z - PV, \quad (3.9)$$

while for the drip phase we have

$$E_{\text{ref,d}}^\mu = \mu_{\text{nd}} N_d + \mu_{\text{pd}} Z_d - P_d V. \quad (3.10)$$

The meaning of E^μ becomes evident if one writes the thermodynamic relation

$$dE = \mu_n dN + \mu_p dZ - P dV, \quad (3.11)$$

where dE is the energy necessary to remove dN neutrons, dZ protons and reduce the volume by an amount dV . Thus, E^μ may be interpreted as a reference disassembly energy [10].

With the help of the equilibrium conditions (2.10)–(2.12) between the nuclear and drip phases, the reference energy for the subtracted system reads

$$\begin{aligned} E_{\text{ref}}^\mu - E_{\text{ref,d}}^\mu &= \mu_n(N - N_d) + \mu_p(Z - Z_d) \\ &= \int_{-\infty}^{\infty} dz \{ \mu_n [\rho_n(z) - \rho_{nd}] + \mu_p [\rho_p(z) - \rho_{pd}] \}. \end{aligned} \quad (3.12)$$

From this equation we can identify a Gibbs reference energy density:

$$\mathcal{E}_{\text{ref}}^\mu(z) = \mu_n [\rho_n(z) - \rho_{nd}] + \mu_p [\rho_p(z) - \rho_{pd}]. \quad (3.13)$$

Substituting Eq. (3.13) into Eq. (3.6), the Gibbs surface tension becomes

$$\sigma_\mu = \int_{-\infty}^{\infty} dz \{ \mathcal{E}(z) - \mathcal{E}_d - \mu_n [\rho_n(z) - \rho_{nd}] - \mu_p [\rho_p(z) - \rho_{pd}] \}. \quad (3.14)$$

As a side remark we note that $\mathcal{E}_{\text{ref}}^\mu(-\infty) = \mathcal{E}_{\text{ref}}^e(-\infty) = \mathcal{E}_0 - \mathcal{E}_d$ and that $\mathcal{E}_{\text{ref}}^\mu(\infty) = \mathcal{E}_{\text{ref}}^e(\infty) = 0$.

Comparing with Eq. (3.1) one concludes that the surface tension that must be minimized for obtaining the density profile is the Gibbs surface tension (3.14). Attempts to minimize the surface tension σ_e , Eq. (3.8), result in the non-conservation of neutrons and protons [49]. Nevertheless, σ_e can be calculated from the variational densities arising from the minimization of σ_μ . Of course, in the case of symmetric semi-infinite nuclear matter, σ_e and σ_μ coincide owing to the Hugenholtz–Van Hove theorem. The surface energy coefficients associated with σ_e and σ_μ are given by

$$E_{\text{s,e}} = 4\pi r_0^2 \sigma_e \quad (3.15)$$

$$E_{\text{s,\mu}} = 4\pi r_0^2 \sigma_\mu, \quad (3.16)$$

where r_0 is the nuclear radius constant:

$$\frac{4}{3}\pi r_0^3 (\rho_0 - \rho_d) = 1. \quad (3.17)$$

Another useful quantity for our study is the so-called surface location z_0 . It is defined as [10]

$$z_0 = \frac{\int_{-\infty}^{\infty} z \rho'(z) dz}{\int_{-\infty}^{\infty} \rho'(z) dz}, \quad (3.18)$$

where the prime denotes a derivative with respect to z . Similar expressions hold for the neutron and proton surface locations (z_{0n} and z_{0p}). It is easy to show that

$$z_0 \Delta \rho = z_{0n} \Delta \rho_n + z_{0p} \Delta \rho_p, \quad (3.19)$$

with $\Delta \rho \equiv \rho_0 - \rho_d$, $\Delta \rho_n \equiv \rho_{n0} - \rho_{nd}$ and $\Delta \rho_p \equiv \rho_{p0} - \rho_{pd}$. After some algebra one obtains an expression relating the two definitions of the surface tension:

$$\sigma_e - \sigma_\mu = (\mu_n - \mu_p)(z_{0n} - z_{0p}) \frac{\Delta \rho_n \Delta \rho_p}{\Delta \rho}. \quad (3.20)$$

In semi-infinite nuclear matter the curvature energy coefficient E_c is given by [1,52,53]

$$\begin{aligned} E_c &= E_c^{\text{geo}} + E_c^{\text{dyn}} \\ E_c^{\text{geo}} &= 8\pi r_0 \int_{-\infty}^{\infty} dz (z - z_0) [\mathcal{E}(z) - \mathcal{E}_d - \mathcal{E}_{\text{ref}}(z)] \\ E_c^{\text{dyn}} &= 8\pi r_0 \int_{-\infty}^{\infty} dz \frac{\partial}{\partial \kappa} [\mathcal{E}(z) - \mathcal{E}_d - \mathcal{E}_{\text{ref}}(z)] \Big|_{\kappa=0}, \end{aligned} \quad (3.21)$$

where κ is the curvature ($\kappa = 2/R$ for a sphere of radius R). The two contributions to the curvature energy coefficient in Eq. (3.21) are called geometrical (E_c^{geo}) and dynamical (E_c^{dyn}) respectively. The geometrical contribution only involves the variation of the surface energy density $\mathcal{E}(z) - \mathcal{E}_d - \mathcal{E}_{\text{ref}}(z)$ across the surface parallel to the z axis. The dynamical part comes from the change of the surface energy density by curvature when the plane surface is infinitesimally bent.

In order to establish a connection between $E_{c,e}^{\text{geo}}$ and $E_{c,\mu}^{\text{geo}}$ it is helpful to define the surface width of the density:

$$b^2 = \frac{\int_{-\infty}^{\infty} (z - z_0)^2 \rho'(z) dz}{\int_{-\infty}^{\infty} \rho'(z) dz}, \quad (3.22)$$

plus similar quantities b_n and b_p for the neutron and proton densities. One finds that b , b_n and b_p satisfy

$$b^2 (\Delta \rho)^2 = b_n^2 \Delta \rho_n \Delta \rho + b_p^2 \Delta \rho_p \Delta \rho + (z_{0n} - z_{0p})^2 \Delta \rho_n \Delta \rho_p. \quad (3.23)$$

Making some calculations it can be shown that

$$\frac{E_{c,e}^{\text{geo}} - E_{c,\mu}^{\text{geo}}}{8\pi r_0} = \frac{(\mu_n - \mu_p) \Delta \rho_n \Delta \rho_p}{2\Delta \rho} \left[b_n^2 - b_p^2 - (z_{0n} - z_{0p})^2 \frac{\Delta \rho_n - \Delta \rho_p}{\Delta \rho} \right]. \quad (3.24)$$

The dynamical part of the curvature energy requires paying a special attention. In general, the surface energy density $\mathcal{E}(z) - \mathcal{E}_d - \mathcal{E}_{\text{ref}}(z)$ depends on the curvature κ in two different manners. First, $\mathcal{E}(z)$ may have an explicit dependence on the laplacian operator Δ which in the limit $R \rightarrow \infty$ reads as $d^2/dz^2 + \kappa d/dz$. Second, the particle densities (and the meson fields in the relativistic case) carry an implicit dependence on the curvature κ . By construction the energy density entering Eq. (3.21) is free from any explicit dependence on the Laplace operator (see Appendix A). Actually, this dependence has been removed by partial integrations in the semiclassical functionals [28,35]. Consequently, in the present calculation, the sole contribution we may have to the dynamical curvature energy comes from the implicit curvature dependence of the nuclear densities and fields. For non-relativistic interactions we find

$$E_c^{\text{dyn}} = 8\pi r_0 \sum_{q=\text{n,p}} \int_{-\infty}^{\infty} dz \left\{ \frac{\delta}{\delta \rho_q} [\mathcal{E}(z) - \mathcal{E}_d - \mathcal{E}_{\text{ref}}(z)] \frac{d\rho_q}{d\kappa} + \frac{\delta}{\delta \rho_{qd}} [\mathcal{E}(z) - \mathcal{E}_d - \mathcal{E}_{\text{ref}}(z)] \frac{d\rho_{qd}}{d\kappa} \right\} \Big|_{\kappa=0}. \quad (3.25)$$

In the relativistic case one has a similar expression but including the variations with respect to the meson fields [9,35].

If we insert in Eq. (3.25) the Gibbs reference energy $\mathcal{E}_{\text{ref}}^\mu(z)$, Eq. (3.13), the prefactors of the derivatives with respect to κ vanish by virtue of the variational equations obeyed by the self-consistent densities (and meson fields), cf. (3.2)–(3.5). Therefore, in our calculation the Gibbs dynamical curvature energy is zero ($E_{c,\mu}^{\text{dyn}} = 0$) and the full Gibbs curvature energy coincides with its geometrical part: $E_{c,\mu} = E_{c,\mu}^{\text{geo}}$.

This is not the situation when one takes the e-definition of the reference energy $\mathcal{E}_{\text{ref}}^e(z)$, Eq. (3.7). In this case one finds a non-zero dynamical curvature energy $E_{c,e}^{\text{dyn}}$, because the prefactors of the derivatives on κ in Eq. (3.25) do not vanish. ($E_{c,e}^{\text{dyn}} = 0$ only for symmetric matter with $\delta_0 = 0$.) Notice that in the relativistic framework there are no contributions from the meson fields to $E_{c,e}^{\text{dyn}}$ (as long as we employ the functionals of Appendix A), since they do not enter in the reference energy.

$E_{c,e}^{\text{dyn}}$ can be recast in the form

$$E_{c,e}^{\text{dyn}} = 8\pi r_0 \int_{-\infty}^{\infty} dz \frac{\partial}{\partial \kappa} [\mathcal{E}(z) - \mathcal{E}_d - \mathcal{E}_{\text{ref}}^\mu(z)] \Big|_{\kappa=0}$$

$$+ 8\pi r_0 \int_{-\infty}^{\infty} dz \frac{\partial}{\partial \kappa} [\mathcal{E}_{\text{ref}}^{\mu}(z) - \mathcal{E}_{\text{ref}}^e(z)] \Big|_{\kappa=0}. \quad (3.26)$$

The first term is just $E_{c,\mu}^{\text{dyn}}$, that vanishes according to the foregoing discussion. As a consequence, the dynamical part of the e-curvature energy can be expressed as

$$E_{c,e}^{\text{dyn}} = 8\pi r_0 \sum_{q=n,p} \left[\mu_q - \frac{\mathcal{E}_0 - \mathcal{E}_d}{\rho_0 - \rho_d} \right] \int_{-\infty}^{\infty} dz \frac{\partial}{\partial \kappa} [\rho_q(z) - \rho_{qd}] \Big|_{\kappa=0}. \quad (3.27)$$

In general the evaluation of $\partial\rho_q/\partial\kappa$ in Eq. (3.27) is not a trivial matter, e.g. it cannot be calculated in a fully quantal way [9]. Fortunately, this problem can be solved within the semiclassical formalism [8,9]. The reason is that the semiclassical expression of the particle density derived from the Wigner–Kirkwood \hbar expansion of the density matrix [3] contains Laplace operators, and thus a dependence on the curvature κ . From the Wigner–Kirkwood density, following Refs. [8] and [9], the dynamical curvature energy $E_{c,e}^{\text{dyn}}$ can be calculated in the ETF and RETF approaches. This is summarized in Appendix B.

4 Discussion of Results

To illustrate our results, we have chosen the Skyrme forces SkM* [54] and SIII [55] as representative interactions for the non-relativistic case, and the non-linear parameter sets NL1 [20], NL2 [56] and NL-SH [57] in the relativistic model. Table 1 collects the saturation properties of nuclear matter for these interactions, plus the droplet model parameters J and L :

$$\begin{aligned}
 J &= \frac{1}{2\rho} \left. \frac{\partial^2 \mathcal{E}(\rho, \delta)}{\partial \delta^2} \right|_{\delta=0, \rho=\rho_{\text{nm}}} \\
 L &= \frac{3\rho}{2} \left. \frac{\partial}{\partial \rho} \frac{\partial^2}{\partial \delta^2} \left(\frac{\mathcal{E}(\rho, \delta)}{\rho} \right) \right|_{\delta=0, \rho=\rho_{\text{nm}}}, \tag{4.1}
 \end{aligned}$$

with ρ_{nm} the saturation density of symmetric nuclear matter. Also given in Table 1 are the values $\bar{\delta}_{\text{nd}}$ and $\bar{\delta}_{\text{pd}}$ of the bulk neutron excess at the neutron and proton drip points.

Although SkM* and SIII resemble in the energy per particle, effective mass m_{∞}^*/m ($\simeq 0.8$) and bulk symmetry energy J ($\simeq 30$ MeV), these forces differ mainly in the incompressibility modulus K (217 MeV for SkM* and 355 MeV for SIII). In the relativistic case, NL1, NL2 and NL-SH also disagree in the value of K : NL1 is similar to SkM*, NL-SH to SIII, and NL2 has the largest K ($\simeq 400$ MeV). The NL1 and NL2 sets have a higher bulk symmetry energy J ($\simeq 45$ MeV) than the Skyrme forces, whereas in NL-SH the value of J is relatively close to SkM*. Concerning the effective mass, in the relativistic sets it is small as compared with the Skyrme forces. For NL1 and NL-SH m_{∞}^*/m is similar ($\simeq 0.6$), while for NL2 it is slightly larger. In any case, notice that the effective mass has a different origin in the relativistic than in the non-relativistic model [58]. All the forces are able to give a reasonably good description of finite nuclei in spite of their differences. In particular, the relativistic set NL-SH is very well suited for nuclei near the neutron drip line [57], that cannot be described so well with other $\sigma-\omega$ sets or Skyrme forces.

4.1 The surface properties

Figure 7 displays the neutron and proton local density profiles obtained from the solution to the Euler–Lagrange equations (3.2)–(3.5) for NL1 and SkM*. They are plotted for several

values of the relative neutron excess in nuclear matter δ_0 . The separation between vertical bars is the surface thickness t , defined as the 90% to 10% fall-off distance. At the top of the figure we show the result for $\delta_0 = 0$, the symmetric semi-infinite geometry. The neutron and proton profiles coincide and the surface region is roughly centered around $z = 0$. The second part of the figure corresponds to $\delta_0 = 0.2$ for which the density profiles begin to differ. The surface thickness for neutrons and protons is very similar to the $\delta_0 = 0$ case. However, while t is still centered around $z = 0$ for the neutron profile, for the proton density t is shifted to negative values of z owing to the symmetry terms of the interaction. The third part of the figure corresponds to $\delta_0 = 0.4$, when drip neutrons have appeared both in NL1 and in SkM*. The surface thickness of the neutron and proton distributions has clearly increased. The density of the drip phase is considerably higher for NL1 than for SkM*, as one would expect from the fact that the neutron drip starts earlier for NL1 (Table 1). Finally, at the bottom of Fig. 7 the profiles are plotted for a high δ_0 beyond the proton drip point. The surface thickness becomes quite large because the interior density and the density of the drip phase are very close.

Figures 8 and 9 offer a more detailed analysis of the surface. They display the surface thickness t and the surface width b , Eq. (3.23), for neutrons and protons calculated with the relativistic sets NL1 and NL2 and with the Skyrme forces SkM* and SIII. One can see that the slope of the t and b curves as a function of δ_0 is steeper for neutrons than for protons. After the neutron drip point, one observes the appearance of a relative maximum (whose height strongly depends on the force) in the surface thickness and width of the neutron density distribution. The presence of this maximum has already been reported in earlier literature [10]. From a qualitative point of view it can be understood as follows. If the bulk symmetry coefficient J is large (as in the σ - ω sets NL1 and NL2), it costs the system a great amount of energy to produce an asymmetry in the bulk, thus favouring the ejection of neutrons to the surface region. However, for a given δ_0 the neutron density in the drip region is fixed by the coexistence equations (2.10)–(2.12). Therefore, if the neutrons pushed out by the symmetry term of the force cannot accommodate in the drip region, they concentrate at the surface and contribute to the development of a maximum in t and b .

This fact is illustrated in Fig. 10, where the number of neutrons per unit area in the surface region N/S is drawn as function of δ_0 for NL2. We have calculated N/S as the integral of the neutron density $\rho_n(z) - \rho_{nd}$ within the 90%–10% fall-off distance. One recognizes that it is immediately after the neutron drip point ($\bar{\delta}_{nd} = 0.222$ for NL2) when the greatest accumulation of neutrons in the surface takes place.

Another quantity of interest for inspecting the surface of the asymmetric system is the neutron skin thickness:

$$\Theta = z_{0n} - z_{0p}, \quad (4.2)$$

where z_{0n} and z_{0p} are the neutron and proton surface locations defined through Eq. (3.18). Figure 11 depicts the change of Θ against δ_0 for our representative forces. For small values of δ_0 the neutron skin thickness behaves linearly, as predicted by the liquid droplet model (LDM) [1]:

$$\Theta = \frac{3r_0}{2} \frac{J}{Q} \delta_0. \quad (4.3)$$

The value of Q , which measures the stiffness of the system against pulling z_{0n} and z_{0p} apart, can be obtained from the slope of Θ at $\delta_0 = 0$. At small δ_0 , forces having a large J/Q ratio have also a large neutron skin thickness. As seen from Fig. 11, for larger δ_0 the neutron skin thickness starts to depart from the linear behaviour and develops a maximum in the region beyond the neutron drip point. This maximum, which also appears in former analyses with non-relativistic forces [10,11], is more pronounced for the relativistic interactions we study here. It is related with the accumulation of neutrons at the surface we have discussed before. With further increase in δ_0 the neutron skin decreases, since the inside and the outside matter become more and more alike and the surface is washed out. At the critical δ_c one expects Θ to eventually vanish.

Figure 12 displays σ_e and σ_μ against δ_0^2 . The surface tension σ_e grows with δ_0^2 and reaches a maximum at some point beyond the neutron drip. Then it falls off to zero as the limiting situation of a uniform system is approached. The Gibbs surface tension shows a different behaviour and it decreases monotonically from its value in the symmetric case to zero. In Figs. 13 and 14 we present our results for the γ_e and γ_μ curvature energies per unit length ($\gamma = E_c/8\pi r_0$). These quantities exhibit a similar behaviour as a function of δ_0^2 to the surface

tensions. NL1 presents a visible peak in γ_e . The dynamical contribution $\gamma_e^{\text{dyn}} = E_{c,e}^{\text{dyn}}/8\pi r_0$ is shown by dashed lines in Figs. 13 and 14. Remember that in our calculation the dynamical curvature energy only differs from zero in the e-definition for $\delta_0 \neq 0$. At high values of δ_0^2 most of the e-curvature energy comes from the dynamical part.

For small values of δ_0 the nuclear droplet model predicts

$$E_{s,e} = E_{s,0} + \left(\frac{9J^2}{4Q} + \frac{2E_{s,0}L}{K} \right) \delta_0^2 \quad (4.4)$$

$$E_{s,\mu} = E_{s,0} - \left(\frac{9J^2}{4Q} - \frac{2E_{s,0}L}{K} \right) \delta_0^2. \quad (4.5)$$

$E_{s,0}$ is the surface energy coefficient for the symmetric case, K is the bulk incompressibility and L reads for the LDM coefficient defined in Eq. (4.1) that gives the density dependence of the symmetry energy. As we realize from Eqs. (4.4) and (4.5), the symmetry contribution to the surface energy in the LDM is positive in the case of the e-definition and negative with the Gibbs prescription. This contribution consists of two terms. The main one ($9J^2/4Q$), represents the variation of the bulk symmetry energy J when the nucleus increases its neutron skin against the resistance provided by the surface stiffness Q . The corrective term $2E_{s,0}L/K$ describes the change of the volume energy produced by a change in the bulk density [1]. While both terms participate additively in the symmetry contribution to $E_{s,e}$, they have opposite signs in $E_{s,\mu}$. Since σ_e and σ_μ must behave according to Eqs. (4.4) and (4.5) for small δ_0^2 , and they must vanish for the uniform system, one can qualitatively understand the global trends of Fig. 12. Apart from using Eq. (4.3) to obtain the surface-stiffness coefficient Q , it can be extracted from the slope of the difference $E_{s,e} - E_{s,\mu}$ that for small values of δ_0 behaves as

$$E_{s,e} - E_{s,\mu} = \frac{9J^2}{2Q} \delta_0^2. \quad (4.6)$$

Table 2 collects E_s , E_c and t computed in the symmetric case ($\delta_0 = 0$) and the coefficient Q , for SkM*, SIII, NL1, NL2 and NL-SH. For the sake of comparison, Table 2 shows in addition results from Refs. [11] and [37]. Our values of the surface-stiffness coefficient calculated from Eqs. (4.3) and (4.6) are in good agreement between them, though small differences arise. In general, the value of Q from Eq. (4.3) is $\sim 0.5 - 1$ MeV greater than the value from Eq. (4.6).

The strength of the peaks that appear in t_n , b_n and Θ in Figs. 8, 9 and 11 is, actually, related with the value of the surface-stiffness coefficient of the force. Comparing with Table 2, one can see that forces with small values of Q have the peaks more developed. As discussed above, such peaks are connected with the neutrons pushed to the surface. Since Q measures the resistance against separating neutrons from protons, it is qualitatively clear that forces having a small Q will tend to concentrate more neutrons at the surface. A similar dependence on Q is observed in the height of the maxima presented by σ_e and γ_e in Figs. 12–14.

From Table 2 we can see that non-relativistic and relativistic parametrizations are able to give comparable surface properties. Nevertheless, for the symmetric case, in Ref. [35] a tendency to thinner density profiles was noticed in the relativistic model, with smaller values of the thickness t when the relativistic interaction was adjusted to give the surface energy of Skyrme forces. Figure 8 suggests that this trend may be reversed at large asymmetries, where t (and b as well, Fig. 9) grows faster with δ_0 for NL1 and NL2 than for SkM* and SIII. To get more insight, we have performed calculations with the relativistic set named RSk1* in Ref. [35]. The parameters of RSk1* were fitted to the nuclear matter properties of SkM* (including the coefficient J), and the scalar mass was chosen to obtain the surface energy of SkM* at $\delta_0 = 0$ in the ETF approach. For RSk1* we find $L = 81.8$ MeV and $Q \approx 25$ MeV, whereas for SkM* it is $L = 45.8$ MeV and $Q \approx 39$ MeV. Observe from this and Tables 1 and 2 an overall tendency of the relativistic sets to have larger L and smaller Q than the Skyrme forces.

Figure 15 summarizes our results for the surface thickness and surface tension with SkM* and RSk1*. The relativistic thickness t is smaller for low neutron excess. But it increases more rapidly with δ_0 and becomes clearly greater than for SkM* at high asymmetries, meaning that the interface disappears sooner in the relativistic case. The height of the relative maximum developed by the surface thickness of the neutron density is larger for RSk1* ($Q \approx 25$ MeV) than for SkM* ($Q \approx 39$ MeV). In Fig. 15 the curves of the Gibbs surface tension σ_μ for RSk1* and SkM* closely follow each other (σ_μ is the minimized quantity in the semi-infinite calculation). At low δ_0 , the surface tension σ_e is larger for the

set RSk1* than for SkM*, while the contrary happens with σ_μ . This is so because of the values of Q for both interactions, as the LDM equations (4.4) and (4.5) show. Since by construction both forces have the same J , the quantity $9J^2/4Q$ is larger for RSk1* and thus the initial slope of the relativistic σ_e and σ_μ is steeper than for SkM*. Altogether, the above hints at a difference in the asymmetry dependence of the nuclear surface in the relativistic model as compared to conventional Skyrme forces.

To conclude this discussion we would like to clarify why the relativistic parametrizations give larger values of L . This fact can be traced back to the behaviour of the symmetry energy with density. From Eq. (4.1) and Appendix A, for Skyrme forces it is

$$J(\rho) = \frac{\hbar^2 k_F^2}{6m} - \frac{1}{4}t_0 \left(\frac{1}{2} + x_0\right)\rho + \frac{1}{24} \left(\frac{3\pi^2}{2}\right)^{2/3} [t_2(4 + 5x_2) - 3t_1x_1] \rho^{5/3} - \frac{1}{24}t_3 \left(\frac{1}{2} + x_3\right) \rho^{1+\alpha}, \quad (4.7)$$

with $k_F = (3\pi^2\rho/2)^{1/3}$. The first term comes from the kinetic energy and the other ones from the interaction. For the considered forces the term with $t_0\rho$ gives a positive contribution, whereas the terms with $\rho^{5/3}$ and $\rho^{1+\alpha}$ produce a negative contribution. The net result is that the function $J(\rho)$ initially grows with density, but it is progressively bent as the density increases. In the relativistic model one has (Appendix A, $\hbar = c = 1$)

$$J(\rho) = \frac{k_F^2}{6\varepsilon_F} + \frac{1}{8} \frac{g_\rho^2}{m_\rho^2} \rho. \quad (4.8)$$

The first quantity is the relativistic kinetic contribution, while the isovector ρ meson is the mechanism of the relativistic interaction to introduce additional symmetry energy. In Eq. (4.8) there are no negative terms that oppose the growing behaviour of $J(\rho)$. Since the coefficient L is essentially the derivative of $J(\rho)$ evaluated at ρ_{nm} , cf. Eq. (4.1), this explains a higher L in the relativistic model.

4.2 Comparison with previous calculations

For the Skyrme forces, our results can be contrasted with those of Kolehmainen *et al.* [11] (KPLT hereafter). Our calculation differs from KPLT in two aspects. On the one

hand, our approach is fully variational whereas in KPLT the densities were restricted to have the form of a trial Fermi function to a power (plus a constant in the case of drip). On the other hand, we have kept the coefficient of the Weizsäcker term in the second-order energy functional equal to its standard ETF value, namely $\beta = 1/36$. However, in several applications of KPLT it was set to $\beta = 1/18$ which somehow simulates effects of order \hbar^4 [4,6]. From Table 2 one can see that, for $\beta = 1/36$, the results obtained in KPLT by means of a parametrized density are very close to those we obtain with fully variational densities (see also Ref. [59]). It is also clear that the use of $\beta = 1/18$ or $\beta = 1/36$ has a drastic effect on the surface properties.

For the SkM* and SIII interactions we may compare our results for the surface tensions σ_e and σ_μ , shown in Fig. 12 as a function of δ_0^2 , with the corresponding values presented in Fig. 7 of KPLT (called σ_s and ω_s respectively). The KPLT calculation was performed for $\beta = 1/18$, but we find a fair agreement between both calculations if our results are scaled by a factor $\sigma_{\text{KPLT},0}/\sigma_0$ (the ratio at $\delta_0 = 0$ of the KPLT value with $\beta = 1/18$ to ours with $\beta = 1/36$, that can be read from Table 2).

From the comparison of Fig. 13 of this work with Fig. 8 of KPLT, we see that the agreement is also good for the Gibbs curvature energy per unit length γ_μ (called ω_c in KPLT), when our results are scaled by $\gamma_{\text{KPLT},0}/\gamma_0$ (it can be read from Table 2). However, a remarkable discrepancy appears when the values for γ_e (called σ_c in KPLT) are compared. After scaling our values with $\gamma_{\text{KPLT},0}/\gamma_0$, they are larger than those reported in KPLT. The disagreement persists if we perform our self-consistent calculation with $\beta = 1/18$. One must note that the authors of KPLT did not include the dynamical curvature energy which comes from the *implicit* curvature dependence of the nuclear densities (see Section 3 and Appendix A of KPLT). This is a non-vanishing contribution in the case of γ_e at $\delta_0 \neq 0$, Eq. (3.27).

In Table 2 we also compare our surface properties for the relativistic model with those reported by Von-Eiff *et al.* [37] (VPSW hereafter). The VPSW results were computed at the TF level, without the gradient corrections we have in the RETF method. For the surface energy coefficient, in the symmetric case, one finds lower values in the RETF than in the TF calculation. As discussed in Refs. [23,28,31,34], this is a typical feature of the relativistic

sets that have a bulk effective mass m_∞^*/m , roughly, below 0.70. From Table 2 we see that the surface thickness t turns out to be smaller in RETF than in TF, in accordance with the trend of the surface energies. Finally, the surface stiffness Q is larger in the RETF calculation than in TF, which expresses a greater rigidity of the nuclear system in RETF against the separation of the neutron and proton surfaces.

4.3 Nuclear matter and the surface in the relativistic model

Next, we analyze the dependence of the surface on the various magnitudes that characterize the infinite nuclear matter in the relativistic case. The saturation properties of nuclear matter are governed by the meson coupling-to-mass ratios g_s^2/m_s^2 , g_v^2/m_v^2 and g_ρ^2/m_ρ^2 , and by the non-linear couplings g_2 and g_3 [12,17] (see Appendix A). Contrarily, the surface properties extracted from the semi-infinite system depend on the meson coupling constants and masses separately.

We start by obtaining the surface properties with a non-linear $\sigma-\omega$ set whose parameters we have fitted to these nuclear matter properties: volume energy $a_v = -16$ MeV, saturation density $\rho_{\text{nm}} = 0.16$ fm $^{-3}$, incompressibility $K = 200$ MeV, effective mass $m_\infty^*/m = 0.70$, and bulk symmetry energy $J = 30$ MeV. The scalar meson mass is $m_s = 500$ MeV. We call this set of parameters NLM. Later we recalculate the surface quantities changing one of the properties that define the set NLM at each time, with the other properties fixed to their initial values. This way we can study the individual effect of each bulk property and of the scalar mass m_s on the surface. The results are collected in Table 3 for the symmetric case $\delta_0 = 0$, and in Table 4 for $\delta_0 = 0.212$ (below neutron drip, corresponding to an ideal system of ^{208}Pb) and $\delta_0 = 0.6$ (above neutron drip).

Table 3 also shows the value of the neutron excess in uniform matter when drip neutrons appear ($\bar{\delta}_{\text{nd}}$) for NLM and the related sets. It can be seen that important changes in $\bar{\delta}_{\text{nd}}$ are connected with varying the volume and symmetry energies. This is due to the fact that the neutron drip is mainly determined by the ratio a_v/J . On the other hand, by decreasing the effective mass or the incompressibility, the neutron drip point moves to higher values of δ_0 . Of course, $\bar{\delta}_{\text{nd}}$ is not changed by variations of m_s that are compensated by changes in

the scalar coupling constant g_s . The proton drip point is less sensitive to the nuclear matter properties and appears at $\delta_0 \sim 0.7$ for all the examined cases, and thus we do not display it in Table 3.

Since the scalar mass sets the range of the attractive scalar interaction, there is a direct correlation between m_s and the surface properties. A larger m_s determines a shorter range of the attractive potential. As Tables 3 and 4 show, this leads to a steeper surface and to a visible reduction of the surface and curvature energies and of the surface thickness t and the neutron skin thickness Θ . The surface also is strongly correlated with the value of the effective mass of the interaction. Indeed, m_∞^*/m plays a prominent role in the majority of nuclear structure properties in the relativistic theory, since it is intimately related to the vector and scalar fields [14,21]. For the symmetric case and small asymmetries, on increasing m_∞^*/m the surface and curvature energy coefficients and t and Θ show a downward trend, as it happened with the scalar mass. The same situation is found at $\delta_0 = 0.6$ except for $E_{s,\mu}$, which turns out to be larger for $m_\infty^*/m = 0.70$ than for $m_\infty^*/m = 0.55$. The effective mass provides a measure of the non-local effects, which contribute to make the surface more diffuse [16]. A higher effective mass is associated with less non-locality and thus it tends to favour a sharper surface.

A smaller value of the incompressibility K softens the nuclear surface and the thickness t augments, while the surface and curvature energies decrease. The change of the neutron skin thickness Θ induced by K is not monotonous with δ_0 . From Tables 3 and 4 it can be checked that the main changes in the ratio E_s/t come from the value of K , as discussed in the literature [17,22]. Increasing K brings about larger E_s/t values. This ratio experiences a clear reduction for high δ_0 . For instance, for the set NLM one has $E_s/t = 8.8$ MeV/fm at $\delta_0 = 0$, 9.1 (6.0) MeV/fm at $\delta_0 = 0.212$, and 3.7 (0.4) MeV/fm at $\delta_0 = 0.6$ (the first number corresponds to $E_{s,e}/t$ and the number in parentheses to $E_{s,\mu}/t$).

Modifying the saturation density ρ_{nm} or the volume energy a_v has little consequences on the surface properties. The analysis of Tables 3 and 4 shows that ρ_{nm} has a moderate effect on the surface and curvature energies, while the surface thickness t is not sensitive to ρ_{nm} . Conversely, the incidence of a_v is more visible on the surface thickness than on the energies.

The neutron skin thickness Θ is almost unaffected by ρ_{nm} and a_v .

The coefficient J does not change the surface properties of the symmetric system. The surface energy $E_{s,e}$ and the neutron skin Θ increase with J at $\delta_0 = 0.212$, but the opposite tendency is found at $\delta_0 = 0.6$. At both values of δ_0 , $E_{c,e}$ and the thickness t become larger when J is raised, whereas $E_{s,\mu}$ and $E_{c,\mu}$ decrease. Reading from Table 3 the value of Q for NLM and for the set with $J = 40$ MeV, the behaviour of Θ , $E_{s,e}$ and $E_{s,\mu}$ with J at $\delta_0 = 0.212$ is consistent with the LDM equations (4.3)–(4.5).

We can see from Table 3 that the surface-stiffness coefficient Q is raised by larger values of m_s , m_∞^*/m and J . This behaviour of Q with m_s and m_∞^*/m is not surprising because the surface becomes stiffer when these quantities increase, and it is harder to separate the neutron and proton surfaces. Furthermore, for small δ_0 at least, it reflects the inverse proportionality between Q and the neutron skin Θ shown by Eq. (4.3), since Θ decreases with m_s and m_∞^*/m (at fixed δ_0). Reducing ρ_{nm} and a_v or a greater K also makes Q grow, but the changes are less noticeable.

In contrast with our finding that Q increases with J when the other properties of the force are not changed, in previous literature increasing values of J have been related with decreasing values of Q [11,37]. Certainly, this is true if the total (bulk-plus-surface) symmetry energy E_{sym} of the interaction is set to the empirical value fitted by mass formulae, that contain a term of the type $a_{\text{sym}}(N - Z)^2/A$. Introducing $I = (N - Z)/A$, in the LDM one has [1]

$$E_{\text{sym}} = a_{\text{sym}} I^2 A = \left[J - \left(\frac{9J^2}{4Q} - \frac{2E_{s,0}L}{K} \right) A^{-1/3} \right] I^2 A, \quad (4.9)$$

which is valid for large A and small I . Equation (4.9) shows that if the symmetry energy E_{sym} of a given interaction is fixed empirically, a large J coefficient must be associated with a small Q coefficient and viceversa. On the contrary, if the parameters of the interaction are not fitted to reproduce E_{sym} such constraint between J and Q needs not be satisfied, as happens e.g. when the parameters are chosen to give the nuclear matter properties we wish.

To clarify this point we plot in Figs. 16 and 17, respectively, the surface-stiffness coefficient Q and the mass-formula symmetry coefficient a_{sym} (calculated for ^{208}Pb) as a function of J . They are drawn for several σ - ω and Skyrme parametrizations; we have added the

relativistic set SRK3M5 ($J = 23.5$ MeV) [31] and the Skyrme force SI' ($J = 29.35$ MeV) [11,60] to the interactions already considered. It can be seen that forces fulfilling that Q decreases as J increases (namely SIII, SI', SkM*, NL-SH and NL1) roughly lie on a curve in the $Q - J$ plane (Fig. 16). These same forces lie in a rather narrow region of values of a_{sym} (22–24 MeV, the empirical region) in the $a_{\text{sym}} - J$ plane (Fig. 17). There are two forces, namely NL2 and SRK3M5, that clearly deviate from the general tendency in the $Q - J$ plane. The reason for this anomaly is that these two forces are clearly outside the empirical region where the remaining forces lie in the $a_{\text{sym}} - J$ plane.

For further insight we have drawn in Figs. 16 and 17 the results of two more forces, NL1J4 and NL1J5. They are identical to the set NL1 excepting the value of the bulk symmetry energy: $J = 40$ MeV for NL1J4 and $J = 50$ MeV for NL1J5. The coefficient a_{sym} for NL1J4 and NL1J5 moves away from the empirical band, but both Q and a_{sym} grow with J because the remaining nuclear matter properties have been kept constant. Thus, to get the right symmetry coefficient a_{sym} one must change various properties of the effective interaction simultaneously, and then the tendency of smaller Q with higher J is fulfilled.

4.4 From semi-infinite matter to finite nuclei

To conclude this section, it may be interesting to compute the energy of large asymmetric and uncharged nuclei using the mass-formula coefficients calculated in the semi-infinite medium. We can then check the results against those we obtain from a self-consistent, semiclassical calculation of spherical finite nuclei [28,31,59] without Coulomb interaction. Before presenting the numbers we pass to discuss some aspects referred to the mass formulae we will utilize.

In writing the energy of a nucleus one has two choices, according to the two definitions of the reference energy, Eqs. (3.7) and (3.12). One possibility is

$$E = E_{\text{v,e}}(\delta_0) A + E_{\text{s,e}}(\delta_0) A^{2/3} + E_{\text{c,e}}(\delta_0) A^{1/3}, \quad (4.10)$$

with an e-volume energy $E_{\text{v,e}} = (\mathcal{E}_0 - \mathcal{E}_d)/(\rho_0 - \rho_d)$, see Eq. (3.7). The other alternative to

write the energy is

$$E = E_{v,\mu}(\delta_0) A + E_{s,\mu}(\delta_0) A^{2/3} + E_{c,\mu}(\delta_0) A^{1/3}, \quad (4.11)$$

in terms of a Gibbs volume energy $E_{v,\mu} = \mu_n(N - N_d)/A + \mu_p(Z - Z_d)/A$, see Eq. (3.12). The surface energy coefficients $E_{s,e}$ and $E_{s,\mu}$ and the curvature energy coefficients $E_{c,e}$ and $E_{c,\mu}$ have been defined in Eqs. (3.15), (3.16) and (3.21).

In order to establish a link with the usual mass formulae we shall restrict ourselves to values of δ_0 below the neutron drip point. In this case $E_{v,e}(\delta_0)$ is just the energy per particle in bulk matter \mathcal{E}/ρ , calculated at the saturation density ρ_{sat} for δ_0 . Likewise, in $E_{v,\mu}(\delta_0)$ the neutron and proton chemical potentials will be evaluated at ρ_{sat} and δ_0 , with $N_d = Z_d = 0$.

When one deals with finite nuclei it must be taken into account that the overall neutron excess I of the system,

$$I = \frac{N - Z}{A}, \quad (4.12)$$

is in general different from the bulk neutron excess δ_0 . Using Eqs. (2.3) and (2.4) the difference between the total volume energies reads

$$\begin{aligned} E_{v,\mu}(\delta_0)A - E_{v,e}(\delta_0)A &= \left(\frac{\partial \mathcal{E}}{\partial \rho} + \frac{\partial \mathcal{E}}{\partial \delta_0} \frac{1 - \delta_0}{\rho} \right) N + \left(\frac{\partial \mathcal{E}}{\partial \rho} - \frac{\partial \mathcal{E}}{\partial \delta_0} \frac{1 + \delta_0}{\rho} \right) Z - \frac{\mathcal{E}}{\rho} A \\ &= \frac{1}{\rho} \frac{\partial \mathcal{E}}{\partial \delta_0} (I - \delta_0) A, \end{aligned} \quad (4.13)$$

with all variables evaluated at the density ρ_{sat} for δ_0 . The Taylor expansion of $E_{v,e}(I)$ about δ_0 gives

$$E_{v,e}(I) = E_{v,e}(\delta_0) + \frac{1}{\rho} \frac{\partial \mathcal{E}}{\partial \delta_0} (I - \delta_0) + \frac{1}{2\rho} \frac{\partial^2 \mathcal{E}}{\partial \delta_0^2} (I - \delta_0)^2 + \dots \quad (4.14)$$

Comparison of Eq. (4.14) with Eq. (4.13) shows that $E_{v,\mu}(\delta_0) - E_{v,e}(I)$ is of second order in the small quantity $I - \delta_0$ and, consequently, one can approach $E_{v,\mu}(\delta_0)$ by $E_{v,e}(I)$. Since in the limit $I \rightarrow 0$ (or $\delta_0 \rightarrow 0$) it is $E_{v,e}(I) = a_v + JI^2$, for small δ_0 and I we can write

$$E_{v,\mu}(\delta_0) = a_v + JI^2. \quad (4.15)$$

Equation (4.13) is actually a surface term (i.e., proportional to $A^{2/3}$). This can be seen as follows. Defining the effective neutron and proton volumes as [10]

$$V_n = \frac{N}{\rho_n} \quad \text{and} \quad V_p = \frac{Z}{\rho_p}, \quad (4.16)$$

one finds

$$\frac{\Delta V}{V} = \frac{V_n - V_p}{V} = \frac{N/\rho_n - Z/\rho_p}{A/\rho} = \frac{2(I - \delta_0)}{1 - \delta_0^2}. \quad (4.17)$$

In the limit of a very large nucleus $\Delta V/V$ can be written as $\Theta S/V$ [10], where S is the surface area and Θ the neutron skin thickness. With $V = 4\pi R^3/3$ and $S = 4\pi R^2$,

$$\frac{\Delta V}{V} = \frac{3\Theta}{R} = \frac{3\Theta}{r_0} A^{-1/3}. \quad (4.18)$$

Combining (4.17) with (4.18) and neglecting δ_0^2 in front of unity leads to

$$I - \delta_0 \simeq \frac{3\Theta}{2r_0} A^{-1/3}, \quad (4.19)$$

which confirms the statement that (4.13) is proportional to $A^{2/3}$.

For small δ_0 , and recalling Eq. (4.3) for Θ , from Eq. (4.19) it is easy to show that the bulk neutron excess δ_0 and the overall neutron excess I are related by

$$\delta_0 \simeq I \left(1 + \frac{9J}{4Q} A^{-1/3} \right)^{-1} \simeq I \left(1 - \frac{9J}{4Q} A^{-1/3} \right), \quad (4.20)$$

provided that $(9J/4Q)A^{-1/3} \ll 1$. This is an interesting result, since it represents a new manner to compute the surface-stiffness coefficient Q , in addition to Eqs. (4.3) and (4.6). By calculating a series of large and uncharged finite nuclei with I constant, and evaluating δ_0 from the central variational densities, from Eq. (4.20) one can extract the value of Q for the considered interaction.

Using the LDM expansion (4.5) for $E_{s,\mu}(\delta_0)$ plus Eq. (4.20), and neglecting asymmetry effects in the curvature energy ($I^2 A^{1/3}$ terms), one recovers from Eq. (4.11) the liquid droplet mass formula for an uncharged nucleus of small asymmetry [1]:

$$\begin{aligned} E &= a_v A + E_{s,0} A^{2/3} + \left(E_{c,0} - \frac{2E_{s,0}^2}{K} \right) A^{1/3} \\ &+ \left[J - \left(\frac{9J^2}{4Q} - \frac{2E_{s,0}L}{K} \right) A^{-1/3} \right] I^2 A. \end{aligned} \quad (4.21)$$

In the above equation $E_{s,0}$ and $E_{c,0}$ are the surface and curvature energy coefficients for the symmetric case, and the corrective term $-(2E_{s,0}^2/K)A^{1/3}$ accounts for the surface compression effects that appear in finite nuclei [1,52]. The formula (4.21) can also be obtained

from Eq. (4.10) by expanding $E_{v,e}(\delta_0)$ as $a_v + J\delta_0^2$ and using Eq. (4.20) together with the expansion (4.4) for $E_{s,e}(\delta_0)$.

Tables 5 and 6 collect the energy per nucleon, obtained in various ways, for uncharged large nuclei using the SkM* and NL2 interactions. The mass number ranges from $A = 250$ to $A = 20000$, while the overall neutron excess is fixed at $I = 0.2$. In both tables we list in the second column $\delta_0(A)$, which we obtain from the interior densities produced by the self-consistent calculation of the finite nucleus with A particles:

$$\delta_0 = \frac{\rho_n(0) - \rho_p(0)}{\rho_n(0) + \rho_p(0)}. \quad (4.22)$$

Note from the tables that δ_0 approaches I as A grows. The energies (per nucleon) of the finite nuclei are given in the third column of Tables 5 and 6, labeled by $E_{\text{FN}}(I)$. In the next two columns we show the predictions of the mass formulae (4.10) and (4.11), labeled by $E_{\text{MF},e}(\delta_0)$ and $E_{\text{MF},\mu}(\delta_0)$ respectively. In both cases we have included an additional term $-(2E_{s,0}^2/K)$ to account for the compressional effect. The rightmost column $E_{\text{LDM}}(I)$ exhibits the output of the LDM mass formula (4.21).

The $E_{\text{MF},\mu}(\delta_0)$ results agree almost perfectly with the self-consistent values $E_{\text{FN}}(I)$ for the largest analyzed nuclei. The differences to $E_{\text{FN}}(I)$ are in all cases smaller than 0.5%, a similar quality to that found in Ref. [35] for a calculation performed in the symmetric case. Though the quality of $E_{\text{MF},e}(\delta_0)$ is also remarkably good, the overall agreement with the self-consistent calculation is a little worse. It was discussed in Section 3 that the surface tension which is minimized in the semi-infinite calculation is the Gibbs surface tension σ_μ , while σ_e is not. The liquid droplet model results also agree very well with $E_{\text{FN}}(I)$, and by extension with $E_{\text{MF},\mu}(\delta_0)$ and $E_{\text{MF},e}(\delta_0)$, as expected from the small value of I . This fact shows that Eqs. (4.10) and (4.11) have the right limit for small δ_0 .

With respect to the LDM mass formula (4.21), Eqs. (4.10) and (4.11) show two main differences. On the one hand, the LDM volume and surface energy coefficients have been expanded up to quadratic terms in asymmetry, while our calculation includes it to all orders. On the other hand, the LDM expression neglects the dependence on asymmetry of the curvature energy term, which we have taken into account in Eqs. (4.10) and (4.11). Looking at each coefficient separately, we have checked that the relative difference (between our

calculation and LDM) is much more important in the curvature energy coefficient than in the other ones. However, due to the A dependence of the mass formula, for very large nuclei most of the final discrepancy between our total energies and the LDM ones comes from the volume and surface terms. This is no longer the case for small nuclei, where the curvature term is mainly responsible for the disagreement.

An advantageous feature of the mass formulae (4.10) and (4.11) with respect to the LDM one is that they also could be employed when drip particles exist. In such a case, one should use the expressions of the e- and μ -volume energies ($E_{v,e}$ and $E_{v,\mu}$) with drip. The compressional energy should be calculated following techniques similar to those of Ref. [61], where this correction was derived at finite temperature for helium clusters.

The neutron skin thickness Θ can be extracted from the finite nuclei results through Eq. (4.19). Reading δ_0 from Tables 5 and 6, we have found a good agreement with reference to the values of Θ calculated in the semi-infinite medium, specially for large A . The agreement worsens slightly if one defines the neutron skin of a finite nucleus to be (see Ref. [6] for a discussion)

$$\Theta = R_n - R_p, \quad (4.23)$$

replacing the actual neutron and proton distributions by spheres of radii R_n and R_p with constant densities $\rho_n(0)$ and $\rho_p(0)$:

$$\begin{aligned} \frac{4}{3}\pi R_n^3 \rho_n(0) &= N \\ \frac{4}{3}\pi R_p^3 \rho_p(0) &= Z. \end{aligned} \quad (4.24)$$

It can be shown that Eq. (4.23) transforms into Eq. (4.19) in the the limit of small asymmetries and to first order in $A^{1/3}$.

As told before, one can calculate Q from the difference $I - \delta_0$ by means of Eq. (4.20). From the values of Tables 5 and 6 we obtain $Q = 39.5$ MeV for SkM* and $Q = 41.9$ MeV for NL2. These results agree nicely with those reported in Table 2 that were obtained directly from the semi-infinite nuclear matter calculations, Eqs. (4.3) and (4.6).

5 Summary

In this paper we have investigated the surface properties of asymmetric semi-infinite nuclear matter with arbitrary neutron excess. This has been done within a semiclassical context, by means of density functional techniques, for non-relativistic and relativistic models. Specifically, we have used the extended Thomas–Fermi approach including gradient corrections of order \hbar^2 , together with Skyrme forces in the non-relativistic case and the non-linear σ – ω model in the relativistic case.

First, we have discussed the coexistence between a nucleus and drip particles under the bulk equilibrium approximation. Next, we have studied the surface properties of two-component systems. We have found the neutron and proton density profiles in the semi-infinite geometry by solving self-consistently the variational Euler–Lagrange equations, at given values of the bulk neutron excess. General trends of the evolution of the nuclear surface with the asymmetry have been obtained by exploring the surface thickness t , the surface width b and the neutron skin thickness Θ .

We have treated the calculation of the surface and curvature energy coefficients according to the two definitions of the reference energy E_{ref} . The self-consistent calculation of the density profiles corresponds to the minimization of the surface tension with the Gibbs prescription for E_{ref} . An important question is the separation of the curvature energy into geometrical and dynamical parts. Though in the Gibbs prescription one can avoid the dynamical term by partial integrations of the Laplacian, there exists always a non-vanishing dynamical contribution at $\delta_0 \neq 0$ if the e-definition of E_{ref} is chosen. We also have calculated the surface stiffness coefficient Q . We have extracted it from the neutron skin Θ and from the surface energy coefficients, finding a good agreement between both methods.

To ascertain the origin of some differences in the surface properties between the non-relativistic and relativistic models, we have built up a non-linear σ – ω parametrization with the same nuclear matter properties and surface energy at zero asymmetry as SkM*. The non-equivalent behaviour in the evolution of the surface with asymmetry is mainly due to the fact that the surface-stiffness coefficient is smaller for the relativistic parametrization.

Comparing our results for Skyrme forces with those of Kolehmainen *et al.* [11] we find

a good correspondence, except for the curvature energy per unit length γ_e for which the implicit curvature dependence was not considered in Ref. [11]. In the relativistic model we could make some comparisons with the Thomas–Fermi results of Von-Eiff *et al.* [37]. For interactions like NL1 and NL-SH with a small effective mass, including the \hbar^2 inhomogeneity corrections reduces the surface energy and thickness, while the surface stiffness Q increases.

Our work has also been concerned with the analysis of the impact on the surface-symmetry properties of the various quantities that characterize the relativistic interaction. The strongest dependences have been found with the scalar mass m_s , that determines the range of the attractive potential, and with the effective mass m_∞^*/m , that somehow reflects the non-local effects.

The surface and curvature coefficients derived in this paper allow to write mass formulae that can be extended to the case when drip particles exist. They could be very useful in physical situations involving large asymmetries. We have checked the predictions of our mass formulae with the self-consistent energies of a calculation of uncharged large finite nuclei, and with the LDM mass formula in the low asymmetry limit. The agreement with the self-consistent calculations is as good as in the symmetric case.

Hot asymmetric nuclear matter and finite nuclei have been investigated in non-relativistic and relativistic calculations. However, to our knowledge, hot semi-infinite nuclear matter has been analyzed only for the symmetric case in the relativistic mean field theory [38]. A natural extension of our work would be to study the surface and curvature properties of asymmetric semi-infinite nuclear matter at finite temperature, since the combined effect of asymmetry and temperature has an important bearing on astrophysical objects and energetic heavy ion collisions.

Acknowledgements

The authors would like to acknowledge support from the DGICYT (Spain) under grant PB95-1249 and from the DGR (Catalonia) under grant GR94-1022. M. Del Estal acknowledges in addition financial support from the CIRIT (Catalonia).

6 Appendix A

In the non-relativistic case with Skyrme forces the energy density for an uncharged nucleus can be written as [4,5]

$$\begin{aligned}
\mathcal{E} = & \frac{\hbar^2}{2m}(f_n\tau_n + f_p\tau_p) + \frac{1}{2}t_0 \left[\left(1 + \frac{x_0}{2}\right) \rho^2 - \left(x_0 + \frac{1}{2}\right) (\rho_n^2 + \rho_p^2) \right] \\
& - \frac{1}{16} \left[t_2 \left(1 + \frac{x_2}{2}\right) - 3t_1 \left(1 + \frac{x_1}{2}\right) \right] (\nabla\rho)^2 \\
& - \frac{1}{16} \left[3t_1 \left(x_1 + \frac{1}{2}\right) + t_2 \left(x_2 + \frac{1}{2}\right) \right] [(\nabla\rho_n)^2 + (\nabla\rho_p)^2] \\
& + \frac{1}{12}t_3\rho^\alpha \left[\left(1 + \frac{x_3}{2}\right) \rho^2 - \left(x_3 + \frac{1}{2}\right) (\rho_n^2 + \rho_p^2) \right] \\
& - \frac{1}{2}W_0 (\rho\nabla\cdot\mathbf{J} + \rho_n\nabla\cdot\mathbf{J}_n + \rho_p\nabla\cdot\mathbf{J}_p). \tag{6.1}
\end{aligned}$$

The quantity f_q ($q = n, p$) is related with the effective mass of each kind of nucleon through

$$\begin{aligned}
f_q = \frac{m}{m_q^*} = & \frac{2m}{\hbar^2} \frac{\partial\mathcal{E}}{\partial\tau_q} = 1 + \frac{m}{2\hbar^2} \left\{ \left[t_1 \left(1 + \frac{x_1}{2}\right) + t_2 \left(1 + \frac{x_2}{2}\right) \right] \rho \right. \\
& \left. + \left[t_2 \left(x_2 + \frac{1}{2}\right) - t_1 \left(x_1 + \frac{1}{2}\right) \right] \rho_q \right\}, \tag{6.2}
\end{aligned}$$

where $\rho = \rho_n + \rho_p$ is the total particle density.

In the ETF approach to order \hbar^2 , the kinetic energy density $f_q\tau_q$ and the spin density \mathbf{J}_q are given by [2,4]

$$f_q\tau_q = \frac{3}{5}(3\pi^2)^{2/3} f_q \rho_q^{5/3} + \frac{1}{36} f_q \frac{(\nabla\rho_q)^2}{\rho_q} - \frac{1}{3} \nabla f_q \cdot \nabla\rho_q - \frac{1}{12} \rho_q \frac{(\nabla f_q)^2}{f_q} + 2\rho_q \frac{(\mathbf{S}_q)^2}{f_q} \tag{6.3}$$

$$\mathbf{J}_q = -\frac{2\rho_q}{f_q} \mathbf{S}_q, \tag{6.4}$$

with

$$\mathbf{S}_q = \frac{m}{2\hbar^2} W_0 (\nabla\rho + \nabla\rho_q). \tag{6.5}$$

In the relativistic formulation, the mean field Hartree energy density for an uncharged nucleus within the non-linear σ - ω model reads [12,20,21]

$$\mathcal{E} = \sum_\alpha \varphi_\alpha^\dagger \left[-i\boldsymbol{\alpha}\cdot\nabla + \beta m^* + g_v V + \frac{1}{2} g_\rho \tau_3 R \right] \varphi_\alpha + \mathcal{E}_f, \tag{6.6}$$

where τ_3 is the third component of the isospin operator and the subindex α runs over occupied shell-model orbitals of the positive energy spectrum. The relativistic effective mass (or Dirac mass) is defined by $m^* = m - g_s\phi$. \mathcal{E}_f represents the additional contribution to the energy density coming from the fields ϕ , V and R associated with the σ , ω and ρ mesons respectively:

$$\begin{aligned}\mathcal{E}_f &= \frac{1}{2} [(\nabla\phi)^2 + m_s^2\phi^2] - \frac{1}{2} [(\nabla V)^2 + m_v^2V^2] - \frac{1}{2} [(\nabla R)^2 + m_\rho^2R^2] \\ &\quad + \frac{1}{3}g_2\phi^3 + \frac{1}{4}g_3\phi^4.\end{aligned}\tag{6.7}$$

In the relativistic expressions we take units $\hbar = c = 1$.

The corresponding semiclassical energy density has a similar structure to Eq. (6.6), except that the nucleon variables are the neutron and proton densities instead of the wave functions. In the RETF approach it reads [28,31]

$$\begin{aligned}\mathcal{E} &= \sum_q \frac{1}{8\pi^2} \left[k_{Fq}\varepsilon_{Fq}^3 + k_{Fq}^3\varepsilon_{Fq} - m^{*4} \ln \frac{k_{Fq} + \varepsilon_{Fq}}{m^*} \right] \\ &\quad + \sum_q \left[B_{1q}(k_{Fq}, m^*)(\nabla\rho_q)^2 + B_{2q}(k_{Fq}, m^*)(\nabla\rho_q \cdot \nabla m^*) \right. \\ &\quad \left. + B_{3q}(k_{Fq}, m^*)(\nabla m^*)^2 \right] + g_v V \rho + \frac{1}{2}g_\rho R(\rho_p - \rho_n) + \mathcal{E}_f.\end{aligned}\tag{6.8}$$

Here $k_{Fq} = (3\pi^2\rho_q)^{1/3}$ is the Fermi momentum and $\varepsilon_{Fq} = \sqrt{k_{Fq}^2 + m^{*2}}$. The functions B_{iq} are the coefficients of the relativistic corrections of order \hbar^2 to the TF model:

$$B_{1q}(k_{Fq}, m^*) = \frac{\pi^2}{24k_{Fq}^3\varepsilon_{Fq}^2} \left(\varepsilon_{Fq} + 2k_{Fq} \ln \frac{k_{Fq} + \varepsilon_{Fq}}{m^*} \right)\tag{6.9}$$

$$B_{2q}(k_{Fq}, m^*) = \frac{m^*}{6k_{Fq}\varepsilon_{Fq}^2} \ln \frac{k_{Fq} + \varepsilon_{Fq}}{m^*}\tag{6.10}$$

$$B_{3q}(k_{Fq}, m^*) = \frac{k_{Fq}^2}{24\pi^2\varepsilon_{Fq}^2} \left[\frac{\varepsilon_{Fq}}{k_{Fq}} - \left(2 + \frac{\varepsilon_{Fq}^2}{k_{Fq}^2} \right) \ln \frac{k_{Fq} + \varepsilon_{Fq}}{m^*} \right].\tag{6.11}$$

We remark that the semiclassical functionals (6.3) and (6.8) do not contain any laplacian operators Δ because they have been removed by suitable partial integrations.

7 Appendix B

The expression (3.27) for $E_{c,e}^{\text{dyn}}$, the dynamical part of the e-curvature energy coefficient, requires the evaluation of the derivatives $\partial\rho_q/\partial\kappa$ (with κ the curvature). We summarize in this appendix how this is achieved. For further details (but restricted to the symmetric problem) we refer the reader to the works [8] and [9]. The starting point is the Wigner–Kirkwood (WK) expansion of the particle density to second order in \hbar . In the non-relativistic case it reads [2,3]

$$\begin{aligned} \rho_{q,\text{nr}}^{\text{WK}} = & \frac{1}{3\pi^2} \left(\frac{2m}{\hbar^2} \right)^{3/2} \left\{ \left(\frac{\mu_q - V_q}{f_q} \right)^{3/2} + \frac{\hbar^2}{16m} \left[\left(\frac{7}{4} \frac{(\nabla f_q)^2}{f_q^2} - 5 \frac{\Delta f_q}{f_q} \right) \left(\frac{\mu_q - V_q}{f_q} \right)^{1/2} \right. \right. \\ & + \left. \left(\frac{1}{2} \frac{(\nabla f_q \cdot \nabla V_q)}{f_q^2} - \frac{\Delta V_q}{f_q} \right) \left(\frac{\mu_q - V_q}{f_q} \right)^{-1/2} \right. \\ & \left. \left. - \frac{1}{4} \frac{(\nabla V_q)^2}{f_q^2} \left(\frac{\mu_q - V_q}{f_q} \right)^{-3/2} \right] \right\}, \end{aligned} \quad (7.1)$$

where $V_q = \delta\mathcal{H}/\delta\rho_q$ is the one-body potential for a Hamiltonian \mathcal{H} .

In the relativistic model we have [28]

$$\begin{aligned} \rho_{q,\text{rel}}^{\text{WK}} = & \frac{k_{\text{F}q}^3}{3\pi^2} + \frac{1}{24\pi^2} \left[\frac{1}{k_{\text{F}q}} \left(3 - \frac{\varepsilon_{\text{F}q}^2}{k_{\text{F}q}^2} \right) (\nabla V_q)^2 - \left(2 \frac{\varepsilon_{\text{F}q}}{k_{\text{F}q}} + 4 \ln \frac{k_{\text{F}q} + \varepsilon_{\text{F}q}}{m^*} \right) \Delta V_q \right. \\ & + 2 \frac{\varepsilon_{\text{F}q}}{k_{\text{F}q} m^*} \left(3 - \frac{\varepsilon_{\text{F}q}^2}{k_{\text{F}q}^2} \right) (\nabla V_q \cdot \nabla m^*) + \frac{1}{k_{\text{F}q}} \left(2 - \frac{\varepsilon_{\text{F}q}^2}{k_{\text{F}q}^2} \right) (\nabla m^*)^2 \\ & \left. - 2 \frac{m^*}{k_{\text{F}q}} \Delta m^* \right], \end{aligned} \quad (7.2)$$

with $k_{\text{F}q}^2 = (\mu_q - V_q)^2 - m^{*2}$ and $V_q = g_v V + g_\rho \tau_3 R/2$ (see Appendix A for notation).

Since in the semi-infinite geometry $\nabla \rightarrow d/dz$ and $\Delta \rightarrow d^2/dz^2 + \kappa d/dz$, one easily finds

$$\frac{\partial\rho_{q,\text{nr}}^{\text{WK}}}{\partial\kappa} = -\frac{1}{24\pi^2} \left(\frac{2m}{\hbar^2} \right)^{1/2} \left[5 \frac{f'_q}{f_q} \left(\frac{\mu_q - V_q}{f_q} \right)^{1/2} + \frac{V'_q}{f_q} \left(\frac{\mu_q - V_q}{f_q} \right)^{-1/2} \right] \quad (7.3)$$

$$\frac{\partial\rho_{q,\text{rel}}^{\text{WK}}}{\partial\kappa} = -\frac{1}{12\pi^2} \left[\left(\frac{\varepsilon_{\text{F}q}}{k_{\text{F}q}} + 2 \ln \frac{k_{\text{F}q} + \varepsilon_{\text{F}q}}{m^*} \right) V'_q + \frac{m^*}{k_{\text{F}q}} m^{*\prime} \right], \quad (7.4)$$

where the primes denote a derivative with respect to z .

Following standard techniques to pass from the WK expressions to the ETF or RETF functionals (see e.g. Refs. [2,3,4,28,34]), it is possible to eliminate algebraically the derivatives of the potential V_q in favour of the derivatives of the density ρ_q and the effective mass. This way, from Eqs. (7.3) and (7.4) one gets the corresponding ETF and RETF contributions:

$$\left(\frac{\partial\rho_q}{\partial\kappa}\right)_{\text{ETF}} = \frac{1}{12\pi^2}(3\pi^2\rho_q)^{1/3}\left(\frac{1}{3}\frac{\rho'_q}{\rho_q} - 2\frac{f'_q}{f_q}\right) \quad (7.5)$$

$$\begin{aligned} \left(\frac{\partial\rho_q}{\partial\kappa}\right)_{\text{RETF}} &= \frac{1}{12\pi^2}\left[\frac{\pi^2}{k_{\text{F}q}^2}\left(1 + 2\frac{k_{\text{F}q}}{\varepsilon_{\text{F}q}}\ln\frac{k_{\text{F}q} + \varepsilon_{\text{F}q}}{m^*}\right)\rho'_q\right. \\ &\quad \left.+ 2\left(\frac{m^*}{\varepsilon_{\text{F}q}}\ln\frac{k_{\text{F}q} + \varepsilon_{\text{F}q}}{m^*}\right)m^{*'}\right]. \end{aligned} \quad (7.6)$$

Finally, replacing these results into Eq. (3.27) one is able to calculate $E_{\text{c,e}}^{\text{dyn}}$ for Skyrme forces and the $\sigma-\omega$ model.

References

- [1] W.D. Myers and W.J. Swiatecki, *Ann. Phys. (N.Y.)* 55 (1969) 395; *Ann. Phys. (N.Y.)* 84 (1974) 186; W.D. Myers, *Droplet model of atomic nuclei* (Plenum, New York, 1977).
- [2] B. Grammaticos and A. Voros, *Ann. Phys. (N.Y.)* 123 (1979) 359; *Ann. Phys. (N.Y.)* 129 (1980) 153.
- [3] P. Ring and P. Schuck, *The nuclear many-body problem* (Springer, New York, 1980) ch. 13.
- [4] M. Brack, C. Guet and H.-B. Håkansson, *Phys. Reports* 123 (1985) 275.
- [5] D. Vautherin and D.M. Brink, *Phys. Rev. C* 5 (1972) 626.
- [6] J. Treiner and H. Krivine, *Ann. Phys. (N.Y.)* 170 (1986) 406.
- [7] W. Stocker, J. Bartel, J.R. Nix and A.J. Sierk, *Nucl. Phys. A* 489 (1988) 252.
- [8] M. Durand, P. Schuck and X. Viñas, *Z. Phys. A* 346 (1993) 87.
- [9] M. Centelles, X. Viñas and P. Schuck, *Phys. Rev. C* 53 (1996) 1018.
- [10] W.D. Myers, W.J. Swiatecki and C.S. Wong, *Nucl. Phys. A* 436 (1985) 185.
- [11] K. Kolehmainen, M. Prakash, J.M. Lattimer and J. Treiner, *Nucl. Phys. A* 439 (1985) 537.
- [12] B.D. Serot and J.D. Walecka, *Adv. Nucl. Phys.* 16 (1986) 1.
- [13] L.S. Celenza and C.M. Shakin, *Relativistic nuclear physics: theories of structure and scattering* (World Scientific, Singapore, 1986).
- [14] P.-G. Reinhard, *Rep. Prog. Phys.* 52 (1989) 439.
- [15] B.D. Serot, *Rep. Prog. Phys.* 55 (1992) 1855.
- [16] J.L. Friar and J.W. Negele, *Adv. Nucl. Phys.* 8 (1975) 219.
- [17] J. Boguta and A.R. Bodmer, *Nucl. Phys. A* 292 (1977) 413.
- [18] C.J. Horowitz and B.D. Serot, *Nucl. Phys. A* 368 (1981) 503.
- [19] A. Bouyssy, S. Marcos and Pham Van Thieu, *Nucl. Phys. A* 422 (1984) 541.
- [20] P.-G. Reinhard, M. Rufa, J. Maruhn, W. Greiner and J. Friedrich, *Z. Phys. A* 323 (1986) 13.

- [21] Y.K. Gambhir, P. Ring and A. Thimet, *Ann. Phys. (N.Y.)* 198 (1990) 132.
- [22] D. Hofer and W. Stocker, *Nucl. Phys. A* 492 (1989) 637.
- [23] D. Von-Eiff, W. Stocker and M.K. Weigel, *Phys. Rev. C* 50 (1994) 1436.
- [24] J. Boguta and J. Rafelski, *Phys. Lett. B* 71 (1977) 22.
- [25] W. Stocker and M.M. Sharma, *Z. Phys. A* 339 (1991) 147.
- [26] M.M. Sharma, S.A. Moszkowski and P. Ring, *Phys. Rev. C* 44 (1991) 2493.
- [27] M. Centelles, X. Viñas, M. Barranco and P. Schuck, *Nucl. Phys. A* 519 (1990) 73c.
- [28] M. Centelles, X. Viñas, M. Barranco and P. Schuck, *Ann. Phys. (N.Y.)* 221 (1993) 165.
- [29] C. Speicher, R.M. Dreizler and E. Engel, *Ann. Phys. (N.Y.)* 213 (1992) 312.
- [30] D. Von-Eiff, S. Haddad and M.K. Weigel, *Phys. Rev. C* 46 (1992) 1797.
- [31] M. Centelles, X. Viñas, M. Barranco, S. Marcos and R.J. Lombard, *Nucl. Phys. A* 537 (1992) 486.
- [32] D. Von-Eiff and M.K. Weigel, *Phys. Rev. C* 46 (1992) 1797.
- [33] M. Centelles, X. Viñas, M. Barranco, N. Ohtsuka, Amand Faessler, Dao T. Khoa and H. Müther, *Phys. Rev. C* 47 (1993) 1091.
- [34] C. Speicher, R.M. Dreizler and E. Engel, *Nucl. Phys. A* 562 (1993) 569.
- [35] M. Centelles and X. Viñas, *Nucl. Phys. A* 563 (1993) 173.
- [36] M. López-Quelle, S. Marcos, R. Niembro, A. Bouyssy and Nguyen Van Giai, *Nucl. Phys. A* 483 (1988) 479.
- [37] D. Von-Eiff, J.M. Pearson, W. Stocker and M.K. Weigel, *Phys. Lett. B* 324 (1994) 279.
- [38] H. Müller and R.M. Dreizler, *Nucl. Phys. A* 563 (1993) 649.
- [39] H. Müller and B.D. Serot, *Phys. Rev. C* 52 (1995) 2072.
- [40] L. Engvik, E. Osnes, M. Hjorth-Jensen, G. Bao and E. Østgaard, *Astrophys. J.* 469 (1996) 794; H. Huber, F. Weber and M.K. Weigel, *Nucl. Phys. A* 596 (1996) 684; H. Müller and B.D. Serot, *Nucl. Phys. A* 606 (1996) 508.
- [41] F. Matera and V. Yu. Denisov, *Phys. Rev. C* 49 (1994) 2816.
- [42] M. Barranco and J. Treiner, *Nucl. Phys. A* 351 (1981) 269.
- [43] P. Bonche, S. Levit and D. Vautherin, *Nucl. Phys. A* 436 (1985) 265.

- [44] E. Suraud, Nucl. Phys. A 462 (1987) 109.
- [45] J.M. Lattimer and D.G. Ravenhall, Ap. J. 223 (1978) 314.
- [46] M. Barranco and J.R. Buchler, Phys. Rev. C 22 (1980) 1729.
- [47] A. Das, R. Nayak and L. Satpathy, J. Phys. G 18 (1992) 869.
- [48] L. Satpathy and R. Nayak, Phys. Rev. Lett. 51 (1983) 1243.
- [49] M. Farine and J.M. Pearson, Phys. Lett. B 167 (1986) 259.
- [50] H.B. Callen, Thermodynamics (Wiley, New York, 1960).
- [51] D.G. Ravenhall, C.D. Bennett and C.J. Pethick, Phys. Rev. Lett. 28 (1972) 978.
- [52] W. Stocker, Nucl. Phys. A 215 (1973) 591.
- [53] W. Stocker and M. Farine, Ann. Phys. (N.Y.) 159 (1985) 255.
- [54] J. Bartel, P. Quentin, M. Brack, C. Guet and H.-B. Håkansson, Nucl. Phys. A 386 (1982) 79.
- [55] M. Beiner, H. Flocard, Nguyen Van Giai and P. Quentin, Nucl. Phys. A 238 (1975) 29.
- [56] S.J. Lee, J. Fink, A.B. Balantekin, M.R. Strayer, A.S. Umar, P.-G. Reinhard, J.A. Maruhn and W. Greiner, Phys. Rev. Lett. 57 (1986) 2916.
- [57] M.M. Sharma, M.A. Nagarajan and P. Ring, Phys. Lett. B 312 (1993) 377.
- [58] M. Jaminon and C. Mahaux, Phys. Rev. C 40 (1989) 354.
- [59] M. Centelles, M. Pi, X. Viñas, F. Garcias and M. Barranco, Nucl. Phys. A 510 (1990) 397.
- [60] J.M. Lattimer, Ann. Rev. Nucl. Part. Sci. 31 (1981) 337.
- [61] A. Guirao, X. Viñas and M. Pi, Z. Phys. D 35 (1995) 199.

Table captions

Table 1. Properties of infinite nuclear matter for the forces used in this work. The last two rows show the values $\bar{\delta}_{\text{nd}}$ and $\bar{\delta}_{\text{pd}}$ of the relative neutron excess at the neutron and proton drip points.

Table 2. Properties of symmetric semi-infinite nuclear matter (surface and curvature energy coefficients E_s and E_c , and surface thickness t), plus the surface-stiffness coefficient Q . The labels (1) and (2) for Q stand for Eqs. (4.3) and (4.6). Besides, we present results from previous works: Ref. [11] (KPLT) and Ref. [37] (VPSW). The calculations of VPSW were performed in the Thomas–Fermi approximation.

Table 3. Change of the surface properties of symmetric matter, and of $\bar{\delta}_{\text{nd}}$ and Q , with the properties of the relativistic interaction. The first row gives the results for the non-linear set NLM. This set is defined by $a_v = -16$ MeV, $\rho_{\text{nm}} = 0.16$ fm $^{-3}$, $K = 200$ MeV, $m_\infty^*/m = 0.70$, $J = 30$ MeV and $m_s = 500$ MeV. (The nucleon and ω - and ρ -meson masses are $m = 939$ MeV, $m_\omega = 783$ MeV and $m_\rho = 763$ MeV.) The next rows correspond to sets of parameters that differ from NLM only by the property listed in the first column.

Table 4. Same as Table 3 for the surface properties of asymmetric matter at $\delta_0 = 0.212$ (below neutron drip) and $\delta_0 = 0.6$ (above neutron drip). Units are MeV for the energies and fm for t and Θ .

Table 5. Energy per nucleon of uncharged large nuclei with mass number A and overall neutron excess $I = 0.2$, for the Skyrme force SkM*. From a semiclassical calculation of finite nuclei we obtain the asymmetry δ_0 at the center of the nucleus, Eq. (4.22), and the energy $E_{\text{FN}}(I)$. $E_{\text{MF},e}(\delta_0)$ and $E_{\text{MF},\mu}(\delta_0)$ are the results of the mass formulae (4.10) and (4.11), including a term $-(2E_{s,0}^2/K)$. Finally, $E_{\text{LDM}}(I)$ is the prediction of the LDM mass formula (4.21).

Table 6. Same as Table 5 for the relativistic set NL2.

Table 1

	SkM*	SIII	NL1	NL2	NL-SH
a_v (MeV)	-15.77	-15.85	-16.42	-17.02	-16.35
ρ_{nm} (fm^{-3})	0.160	0.145	0.152	0.146	0.146
K (MeV)	216.6	355.4	211.1	399.2	355.3
m_{∞}^*/m	0.789	0.763	0.573	0.670	0.598
J (MeV)	30.03	28.16	43.46	45.12	36.12
L (MeV)	45.8	9.9	140.2	133.4	113.7
$\bar{\delta}_{\text{nd}}$	0.322	0.337	0.240	0.222	0.284
$\bar{\delta}_{\text{pd}}$	0.820	0.970	0.637	0.749	0.714

Table 2

	SkM*	SIII	NL1	NL2	NL-SH
<i>E_s</i> (MeV)					
this work	16.00	16.47	17.38	19.65	17.22
KPLT (1/36)	16.05	16.55			
KPLT (1/18)	17.96	18.79			
VPSW (TF)			19.78		20.07
<i>E_c</i> (MeV)					
this work	10.53	7.33	12.59	9.10	8.40
KPLT (1/36)	10.74	7.50			
KPLT (1/18)	13.87	10.10			
<i>t</i> (fm)					
this work	2.23	1.72	2.11	1.50	1.50
KPLT (1/36)	2.26	1.75			
KPLT (1/18)	2.45	1.93			
VPSW (TF)			2.90		2.09
<i>Q</i> (MeV)					
this work (1)	39.6	63.8	29.8	41.9	34.7
this work (2)	38.4	63.3	29.0	41.6	34.2
KPLT (1/36)	38	61			
KPLT (1/18)	34	54			
VPSW (TF)			24.4		27.6

Table 3

	$\bar{\delta}_{\text{nd}}$	$\delta_0 = 0$			
		E_s (MeV)	E_c (MeV)	t (fm)	Q (MeV)
Set NLM	0.385	14.81	9.53	1.68	28.8
$a_v = -17$ MeV	0.439	14.67	9.26	1.59	30.4
$\rho_{\text{nm}} = 0.145$ fm ⁻³	0.387	14.29	8.88	1.68	29.4
$K = 300$ MeV	0.355	17.56	9.61	1.61	30.0
$m_\infty^*/m = 0.55$	0.446	16.54	12.01	2.03	22.2
$J = 40$ MeV	0.252	14.81	9.53	1.68	35.0
$m_s = 550$ MeV	0.385	11.82	6.05	1.18	38.4

Table 4

	$\delta_0 = 0.212$						$\delta_0 = 0.6$					
	$E_{s,e}$	$E_{c,e}$	$E_{s,\mu}$	$E_{c,\mu}$	t	Θ	$E_{s,e}$	$E_{c,e}$	$E_{s,\mu}$	$E_{c,\mu}$	t	Θ
Set NLM	18.7	11.6	12.4	8.1	2.06	0.43	17.0	18.8	1.65	1.00	4.63	0.70
$a_v = -17$ MeV	18.4	11.2	12.4	8.0	1.94	0.40	17.0	18.5	1.64	0.95	4.45	0.70
$\rho_{\text{nm}} = 0.145$ fm ⁻³	18.1	10.9	11.9	7.5	2.06	0.43	16.0	17.9	1.58	0.94	4.63	0.68
$K = 300$ MeV	21.2	11.6	15.0	8.1	1.94	0.41	22.6	24.7	2.41	1.01	4.17	0.82
$m_\infty^*/m = 0.55$	21.7	15.1	13.6	10.6	2.58	0.56	19.3	21.4	1.58	1.23	6.20	0.91
$J = 40$ MeV	21.0	14.4	11.2	6.8	2.26	0.51	15.1	19.2	1.40	0.99	4.89	0.48
$m_s = 550$ MeV	14.9	8.4	10.0	5.4	1.51	0.33	13.8	15.2	1.36	0.73	3.69	0.56

Table 5

SkM* ($I = 0.2$)					
A	δ_0	$E_{\text{FN}}(I)$	$E_{\text{MF,e}}(\delta_0)$	$E_{\text{MF},\mu}(\delta_0)$	$E_{\text{LDM}}(I)$
250	0.152	-12.129	-12.124	-12.171	-12.111
500	0.160	-12.664	-12.667	-12.652	-12.561
1000	0.168	-13.080	-13.085	-13.074	-13.068
5000	0.180	-13.723	-13.728	-13.722	-13.711
10000	0.184	-13.905	-13.909	-13.904	-13.892
20000	0.187	-14.047	-14.049	-14.047	-14.035

Table 6

NL2 ($I = 0.2$)					
A	δ_0	$E_{\text{FN}}(I)$	$E_{\text{MF,e}}(\delta_0)$	$E_{\text{MF},\mu}(\delta_0)$	$E_{\text{LDM}}(I)$
250	0.137	-12.447	-12.456	-12.422	-12.530
500	0.147	-13.064	-13.079	-13.052	-13.111
1000	0.156	-13.540	-13.554	-13.534	-13.564
5000	0.172	-14.276	-14.285	-14.275	-14.267
10000	0.177	-14.483	-14.493	-14.482	-14.466
20000	0.181	-14.646	-14.659	-14.646	-14.624

Figure captions

Figure 1. Neutron and proton chemical potentials of bulk matter (μ_n and μ_p) as a function of the relative neutron excess δ , for the relativistic interaction NL1. The vertical slashes indicate the neutron and proton drip points ($\bar{\delta}_{nd}$ and $\bar{\delta}_{pd}$) and the critical point (δ_c) where the densities of the two phases become equal. For $\delta < \delta_c$ it is $\delta = \delta_0$, the neutron excess of the nuclear phase. When proton drip occurs ($\delta_d < 1$) the dashed lines allow one to read the neutron excess δ_d of the drip phase that is in equilibrium with the nuclear phase at δ_0 .

Figure 2. Same as Fig. 1 for the densities of the nuclear and drip phases, ρ_0 and ρ_d , against δ^2 . The superimposed dot-dashed lines illustrate an example of coexistence between a nuclear medium with $\delta_0^2 = 0.6$ and density $\rho_0 = 0.082 \text{ fm}^{-3}$ and drip matter with $\delta_d^2 = 0.9$ and density $\rho_d = 0.064 \text{ fm}^{-3}$.

Figure 3. Equation of state for the NL1 parametrization. The solid lines represent the pressure P as a function of the density ρ for several values of δ (from the neutron drip point to neutron matter). The dot-dashed line defines the coexistence curve. The long-dashed and short-dashed lines are the diffusive and mechanical stability curves. Some samples of points on the coexistence curve that can be in phase equilibrium have been joined by dashed lines.

Figure 4. Same as Fig. 3 for the neutron chemical potential μ_n .

Figure 5. Same as Fig. 3 for the proton chemical potential μ_p .

Figure 6. Schematic representation of the density profile $\rho(z)$ of the semi-infinite system with drip particles. The quantities ρ_0 and ρ_d are the asymptotic densities when $z \rightarrow -\infty$ and $z \rightarrow \infty$, respectively.

Figure 7. Neutron and proton local density profiles of semi-infinite matter for the relativistic set NL1 and the Skyrme force SkM*. They are drawn for several bulk asymmetries: $\delta_0 = 0$ (symmetric system), $\delta_0 = 0.24$ (below neutron drip), $\delta_0 = 0.4$ (above neutron

drip), and finally at a δ_0 above proton drip. For the asymmetric cases the lower curves are the proton densities. The vertical bars show the surface thickness t , the distance where the density of the nucleus drops from 90% to 10% of its central value.

Figure 8. Surface thickness t of the neutron (n) and proton (p) density distributions against the bulk neutron excess δ_0 for the relativistic sets NL1 and NL2 and for the Skyrme forces SkM* and SIII.

Figure 9. Same as Fig. 8 for the surface width b of the neutron and proton density distributions.

Figure 10. Number of neutrons per unit area in the surface region (see text for explanation) as a function of δ_0 for the NL2 parametrization. The vertical line indicates the neutron drip point.

Figure 11. Neutron skin thickness Θ versus δ_0 .

Figure 12. Dependence of the surface tension upon δ_0^2 for the two definitions of the reference energy discussed in the text.

Figure 13. Dependence of the curvature energies per unit length γ_e and γ_μ upon δ_0^2 for SkM* and SIII. The dashed lines show the dynamical contribution γ_e^{dyn} .

Figure 14. Same as Fig. 13 for the relativistic sets NL1 and NL2.

Figure 15. Surface tension and surface thickness for SkM* and for the relativistic set RSk1* adjusted to the nuclear matter properties and surface energy at $\delta_0 = 0$ of SkM*.

Figure 16. Surface-stiffness coefficient Q against the bulk symmetry energy J for some relativistic and non-relativistic parametrizations.

Figure 17. Mass-formula symmetry coefficient a_{sym} calculated for ^{208}Pb , Eq. (4.9), against the bulk symmetry energy J for the forces of Fig. 16. The dashed lines roughly indicate the empirical region.

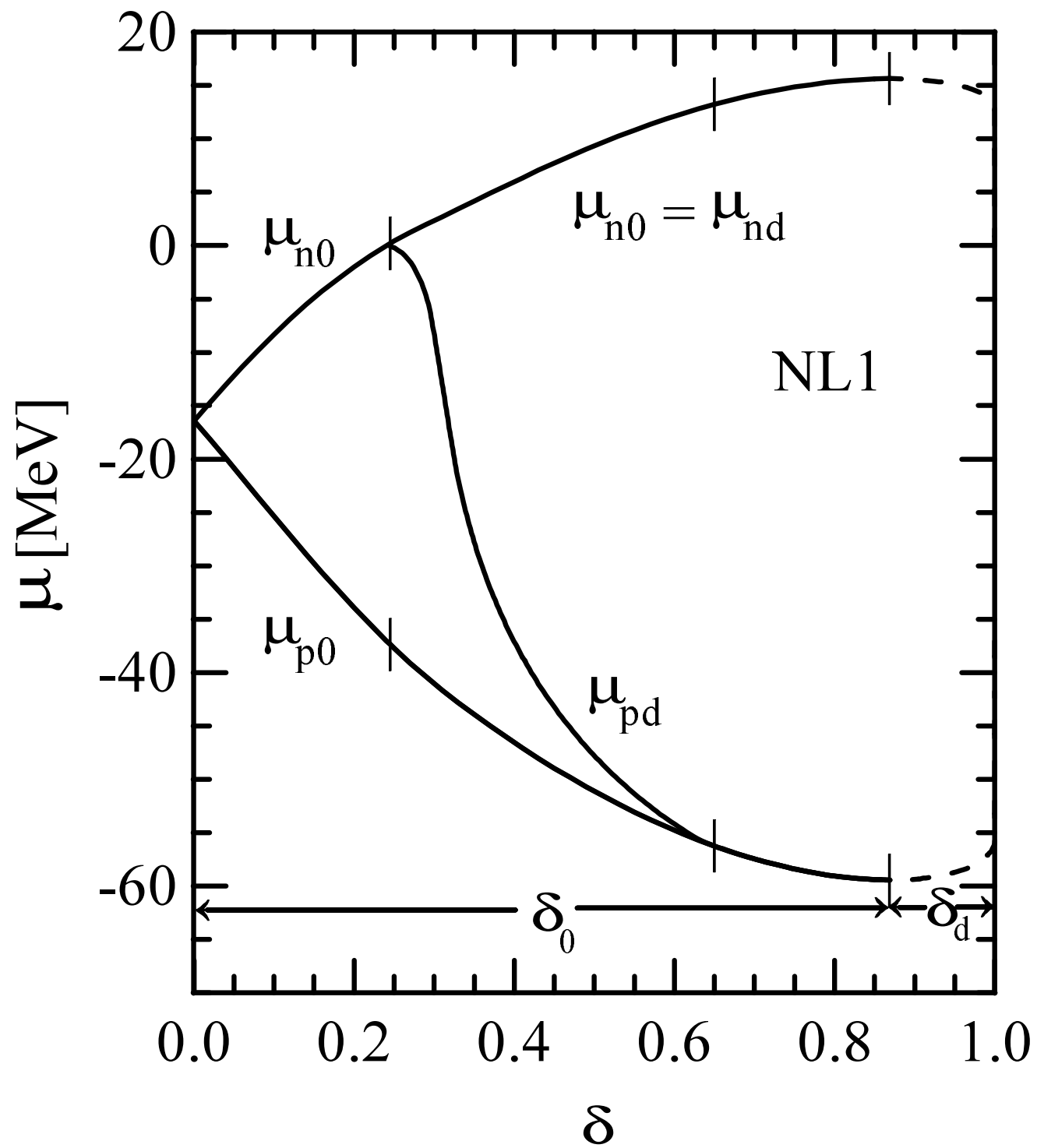


Figure 2

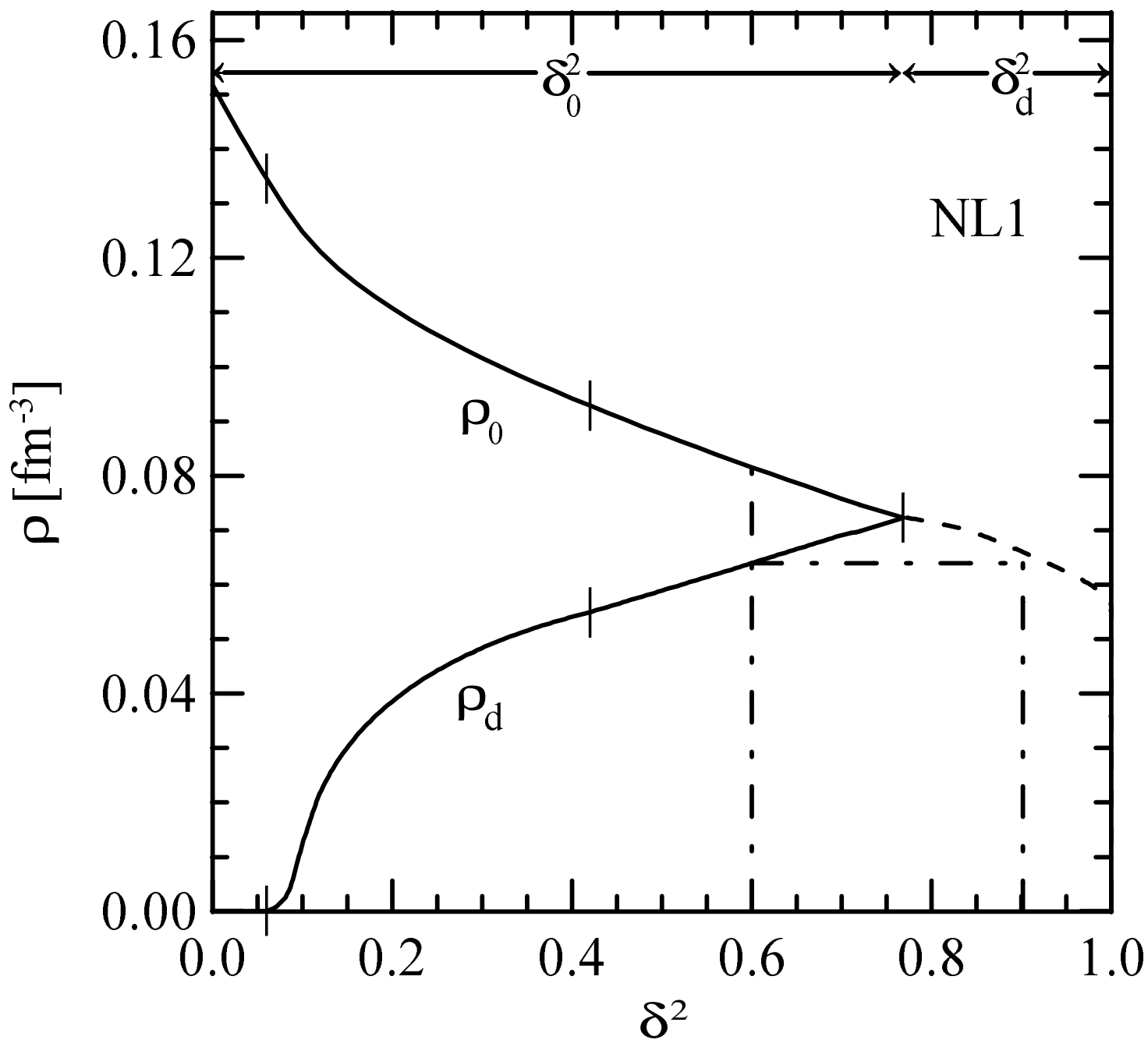


Figure 3

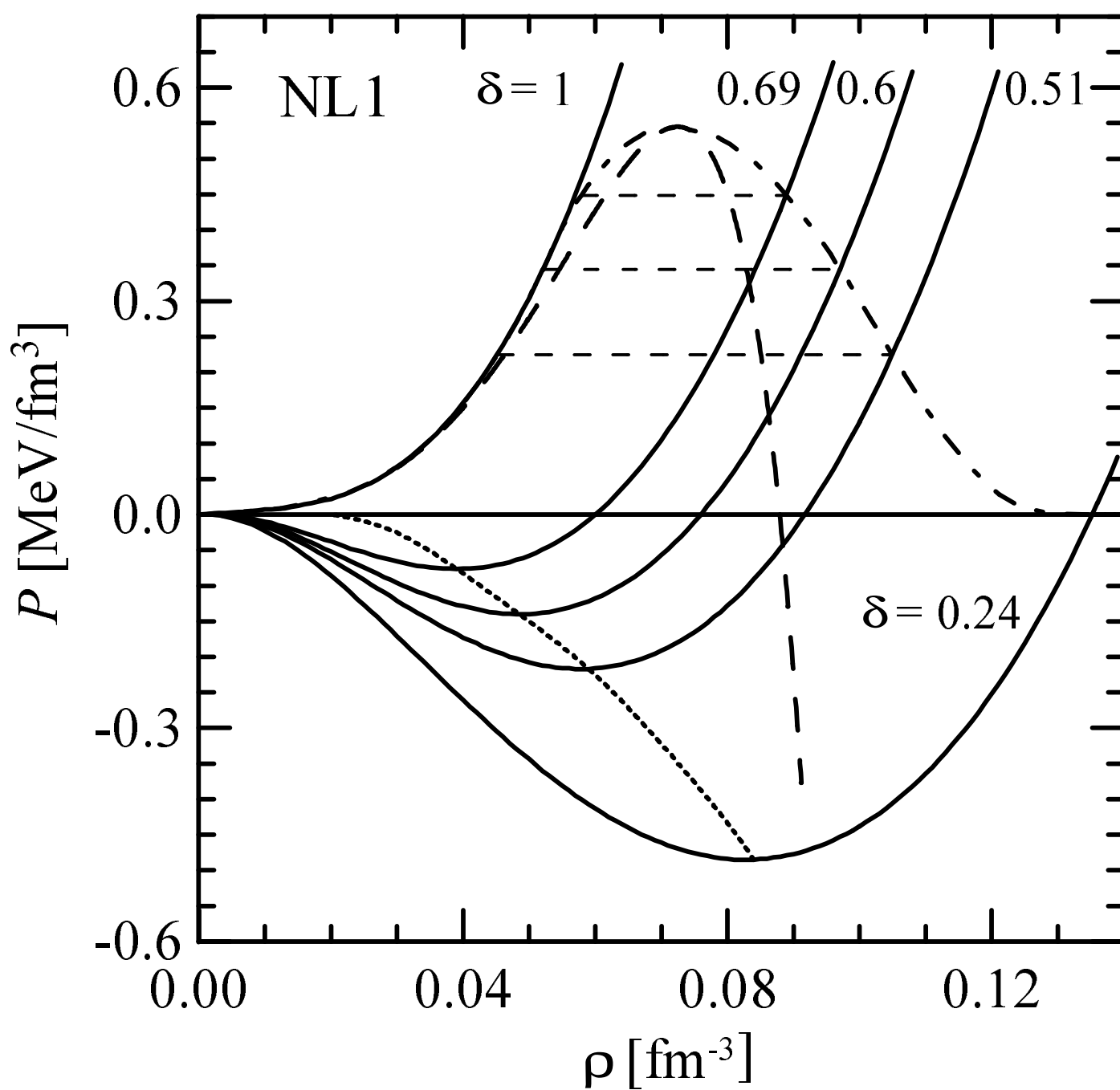


Figure 4

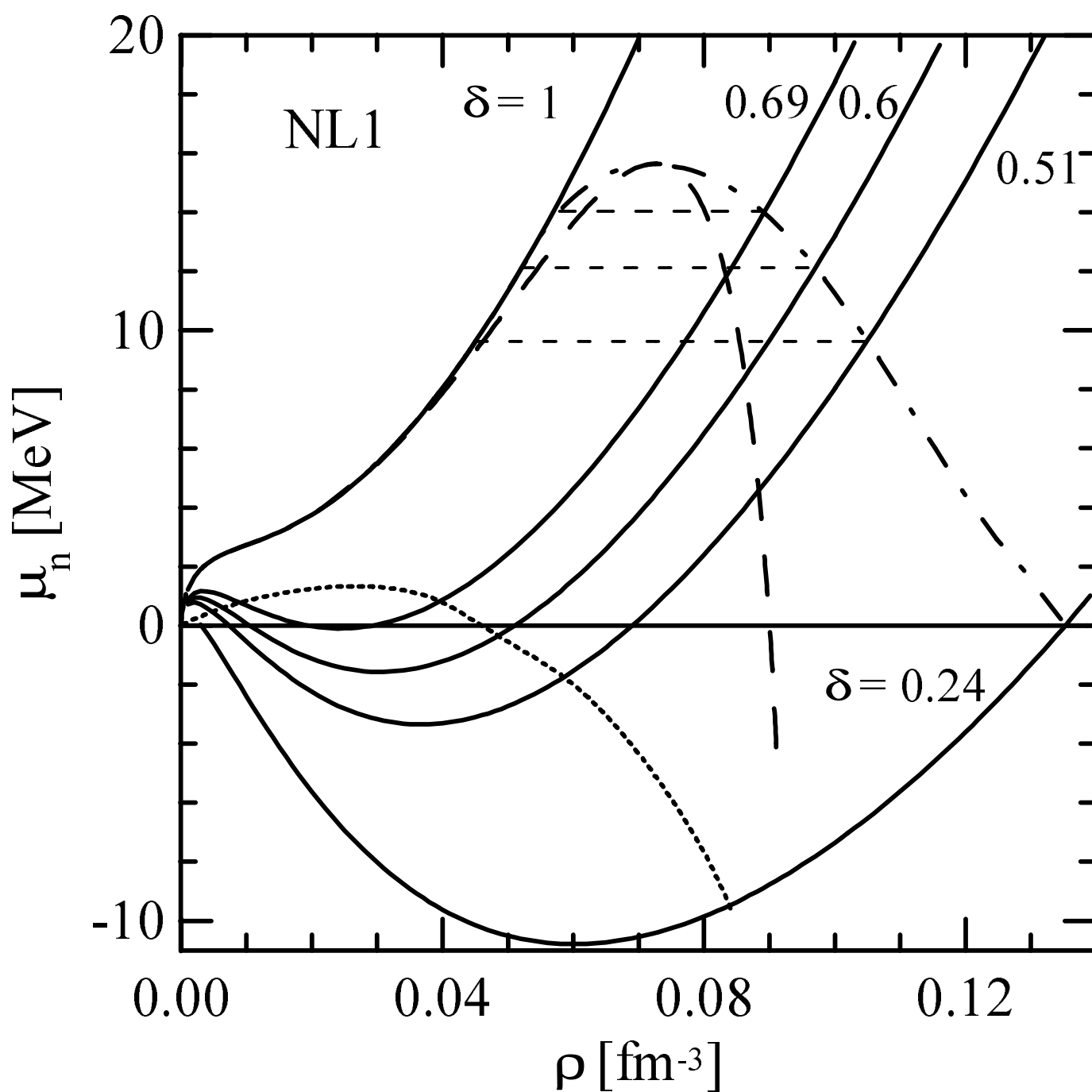


Figure 5

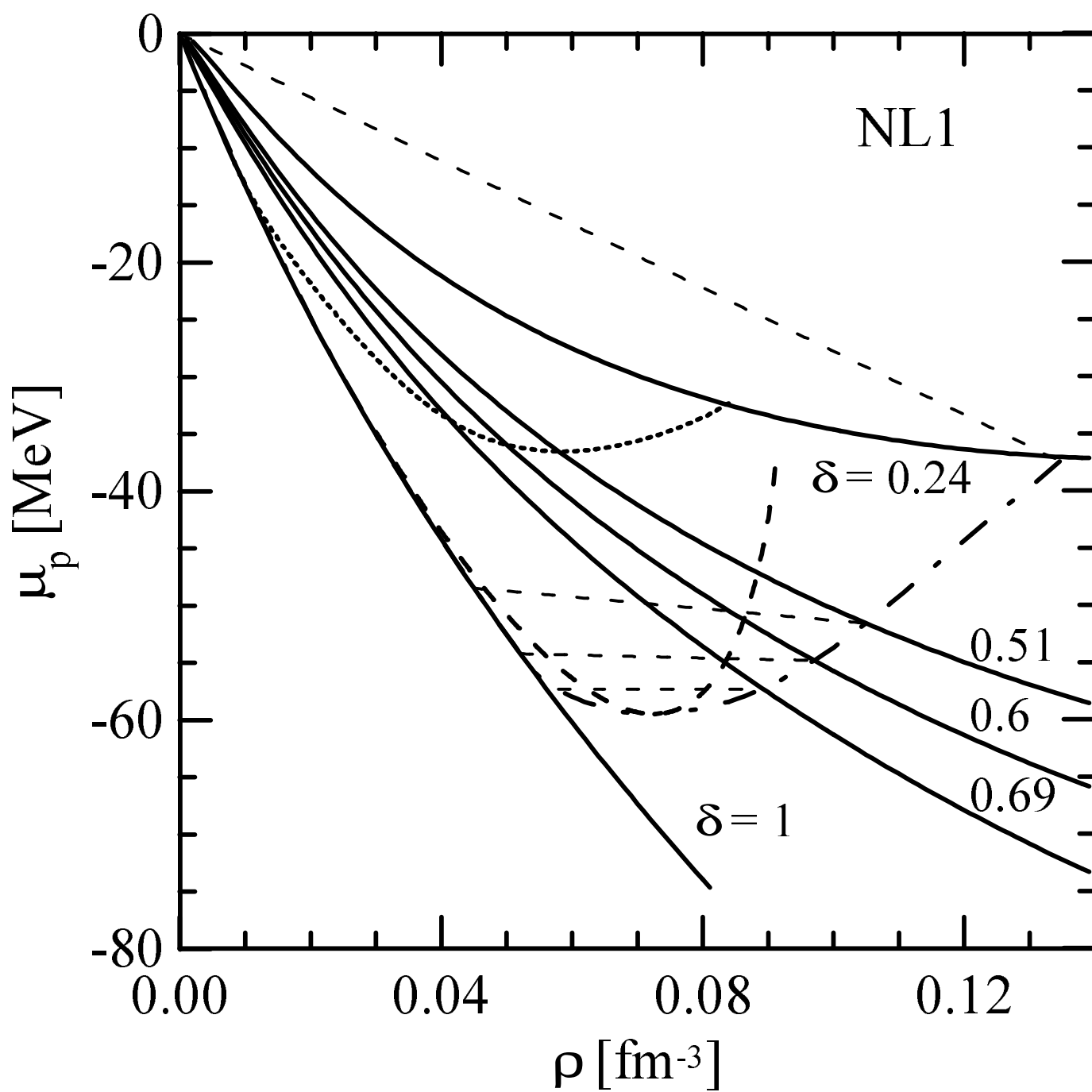
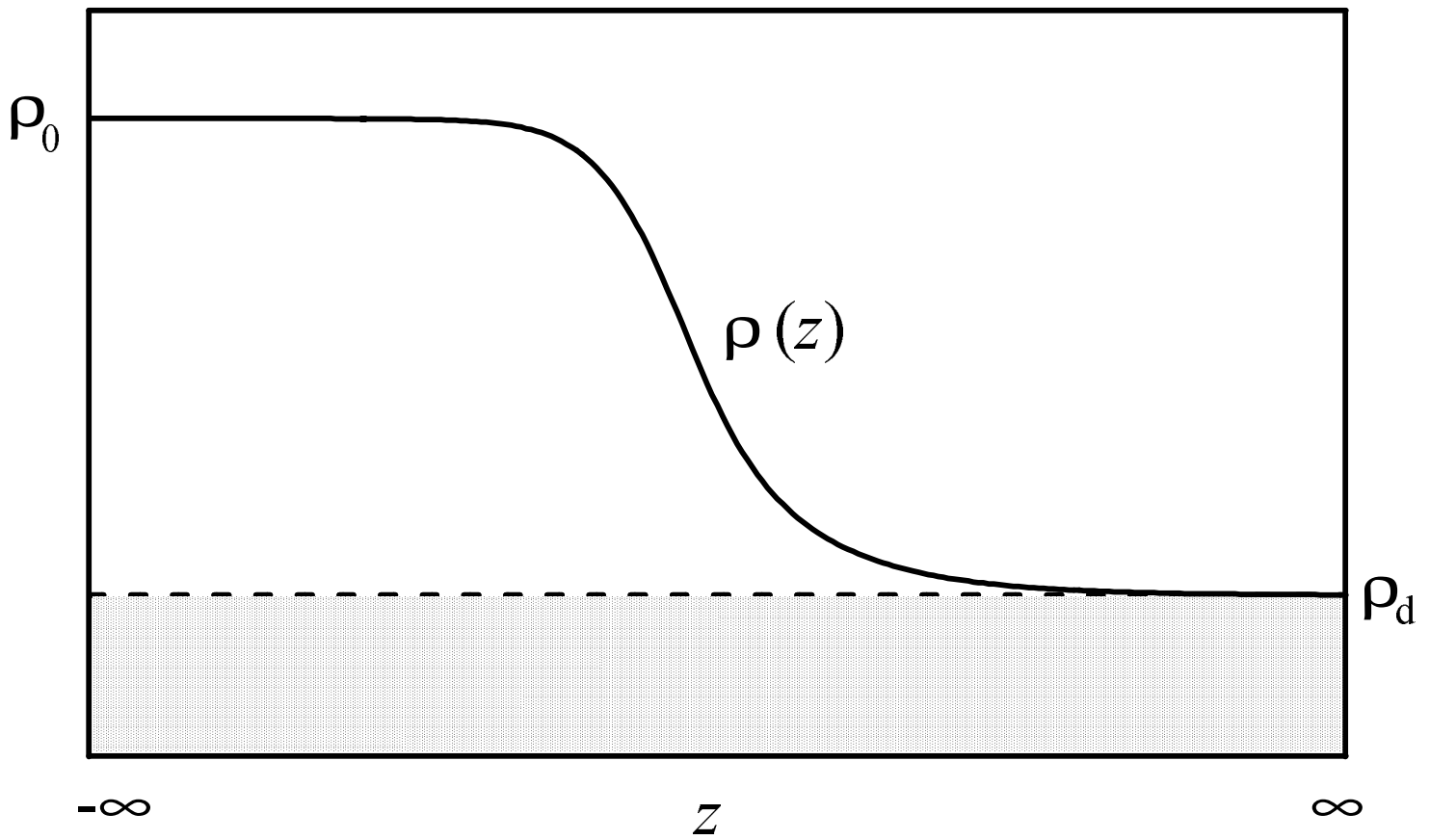


Figure 6



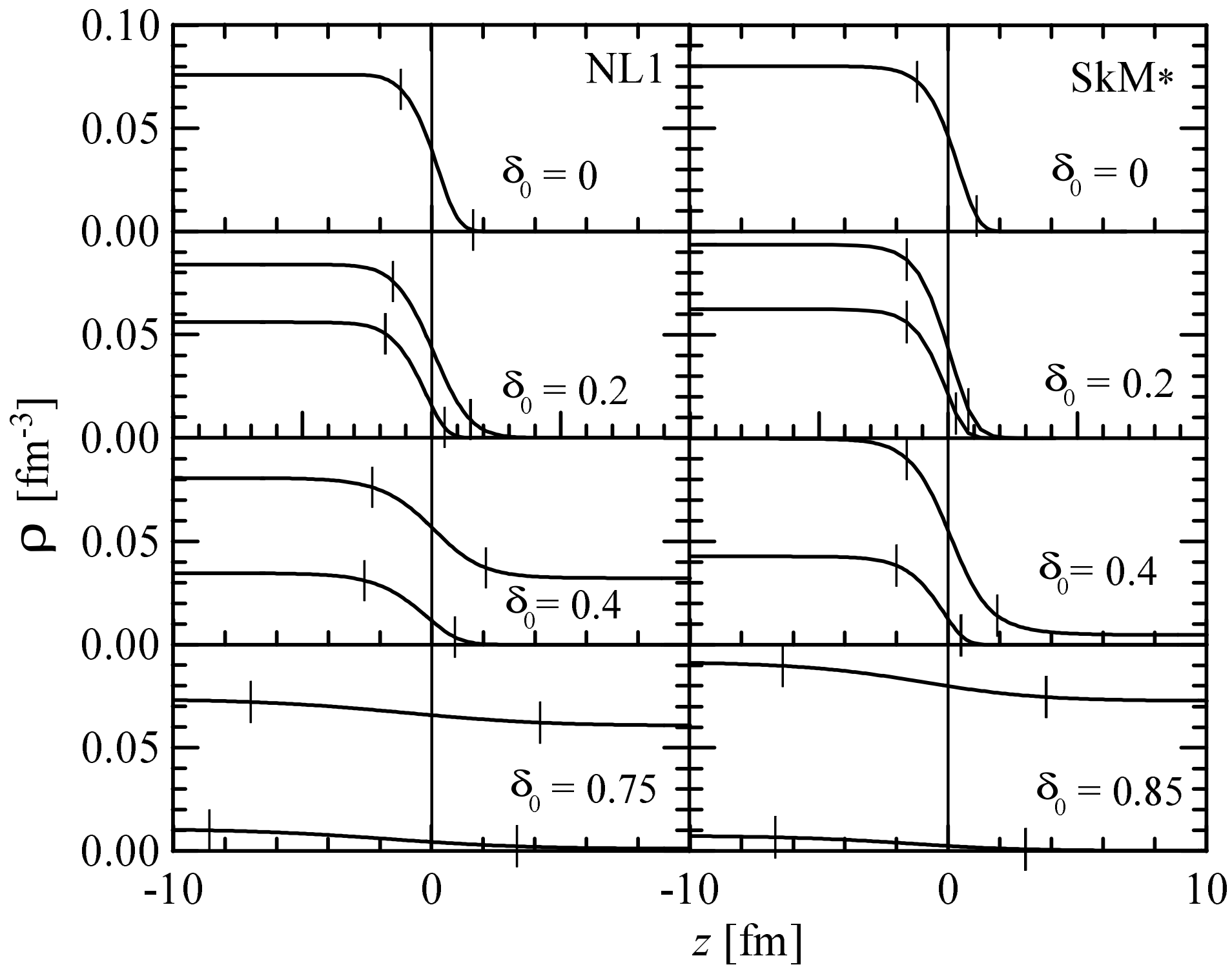


Figure 8

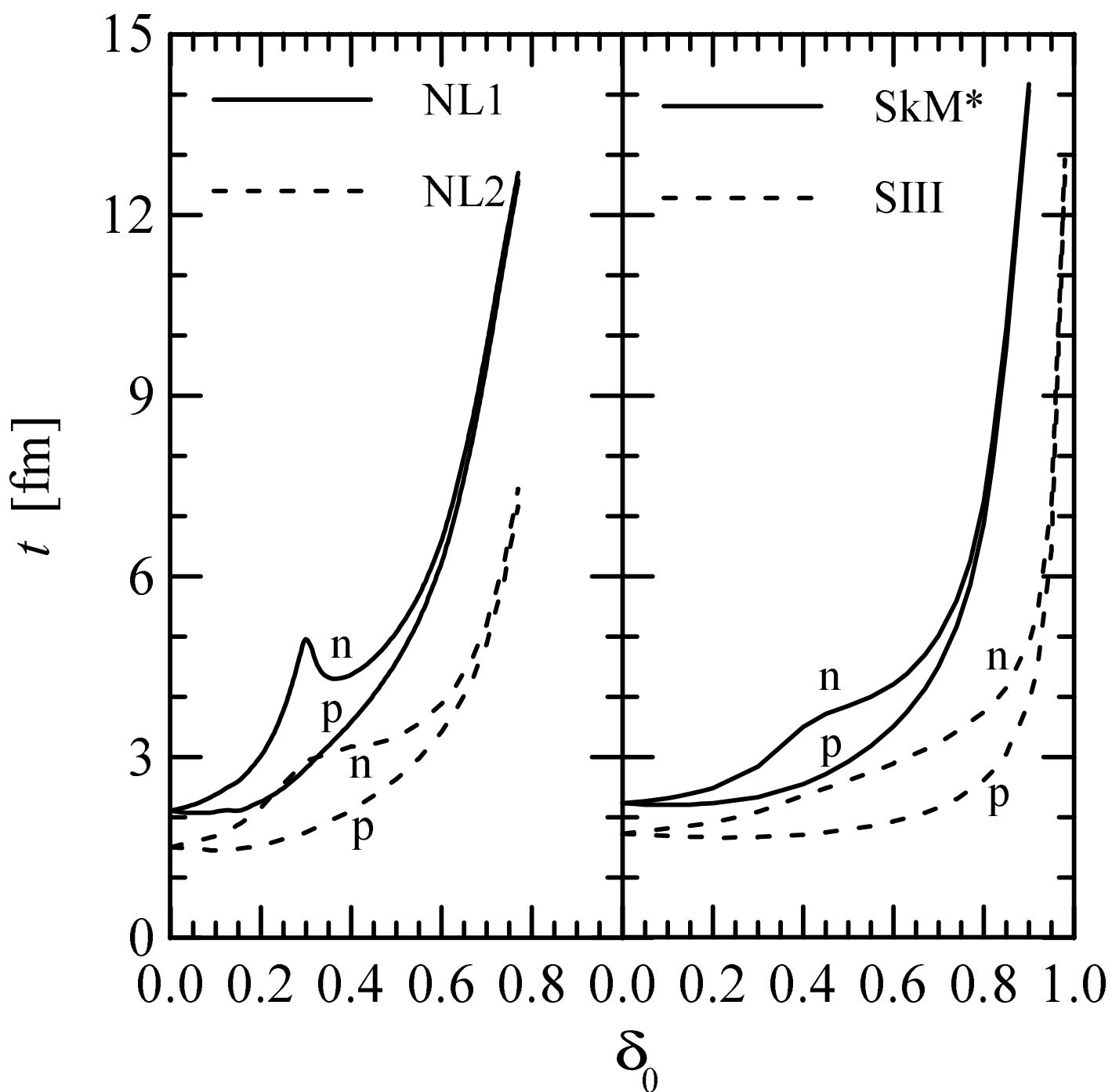


Figure 9

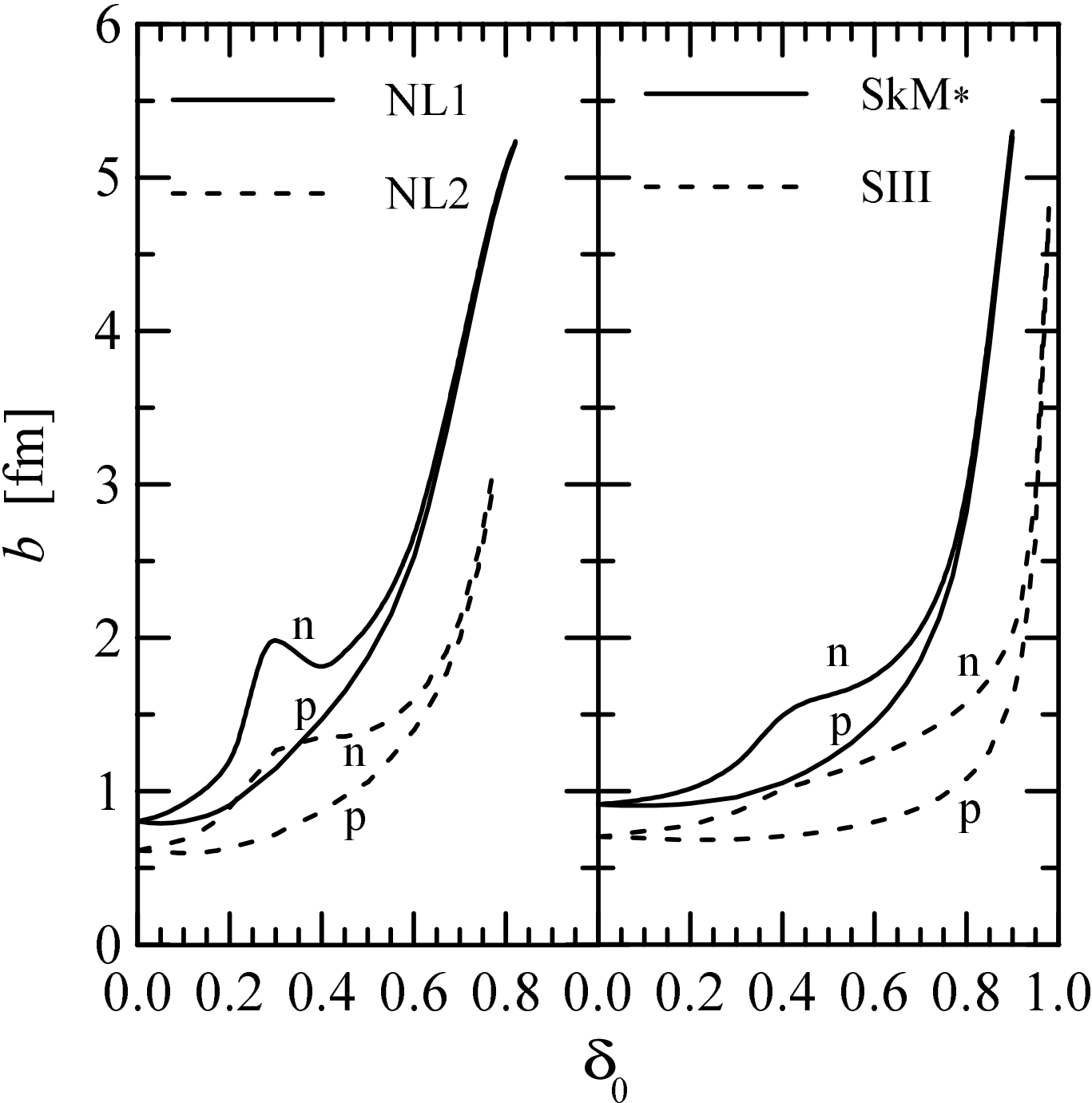


Figure 10

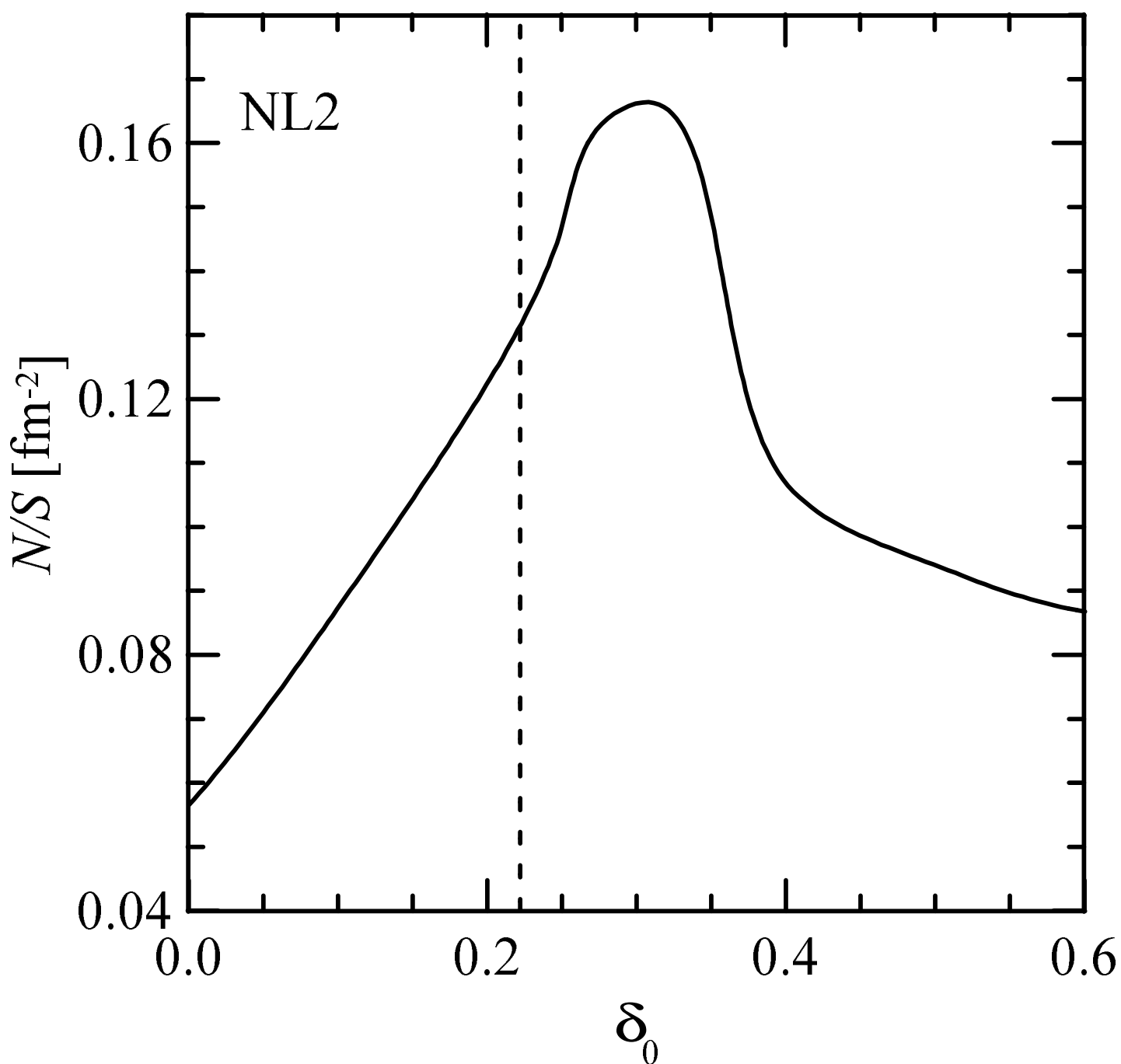


Figure 11

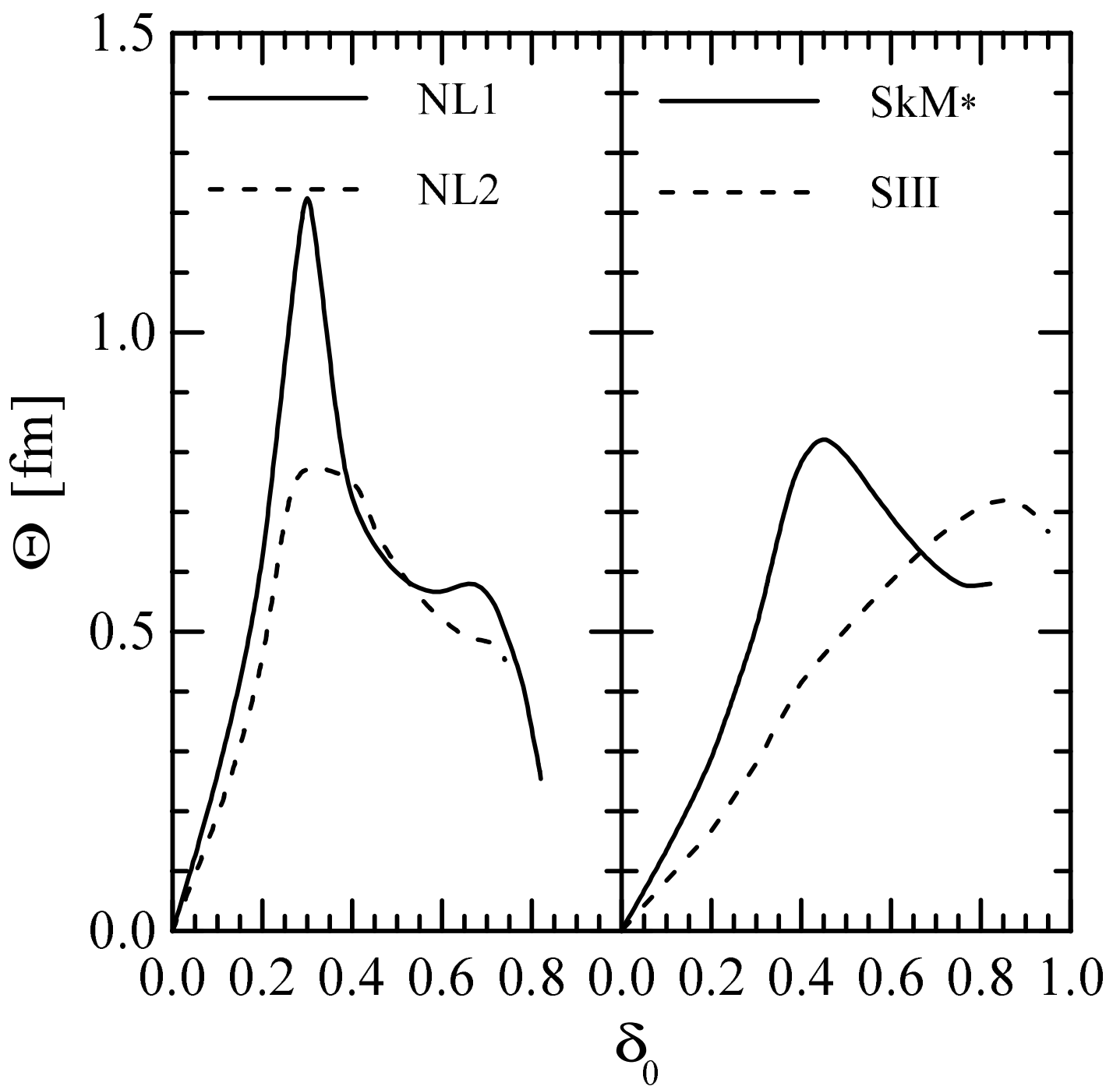


Figure 12

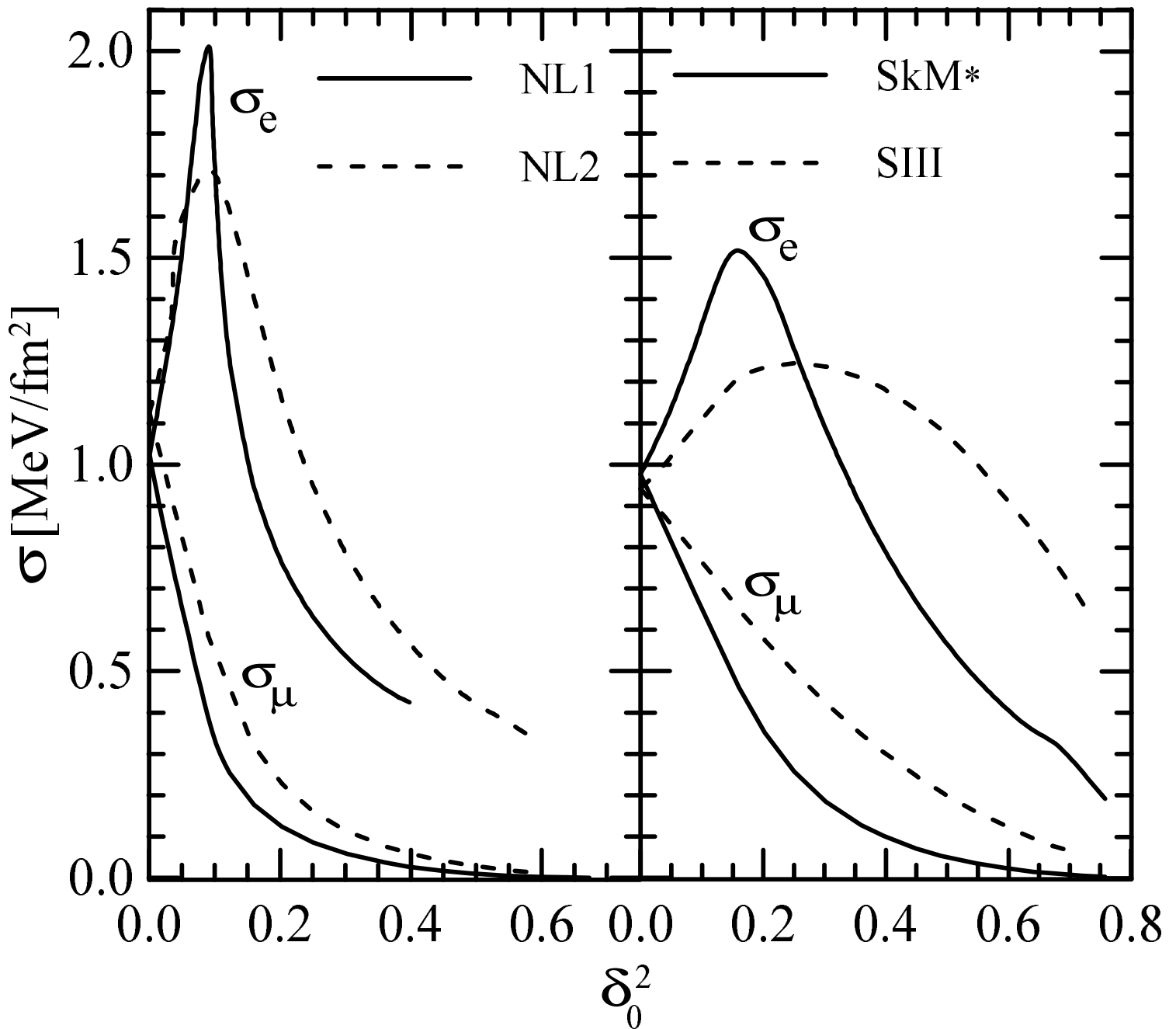


Figure 13

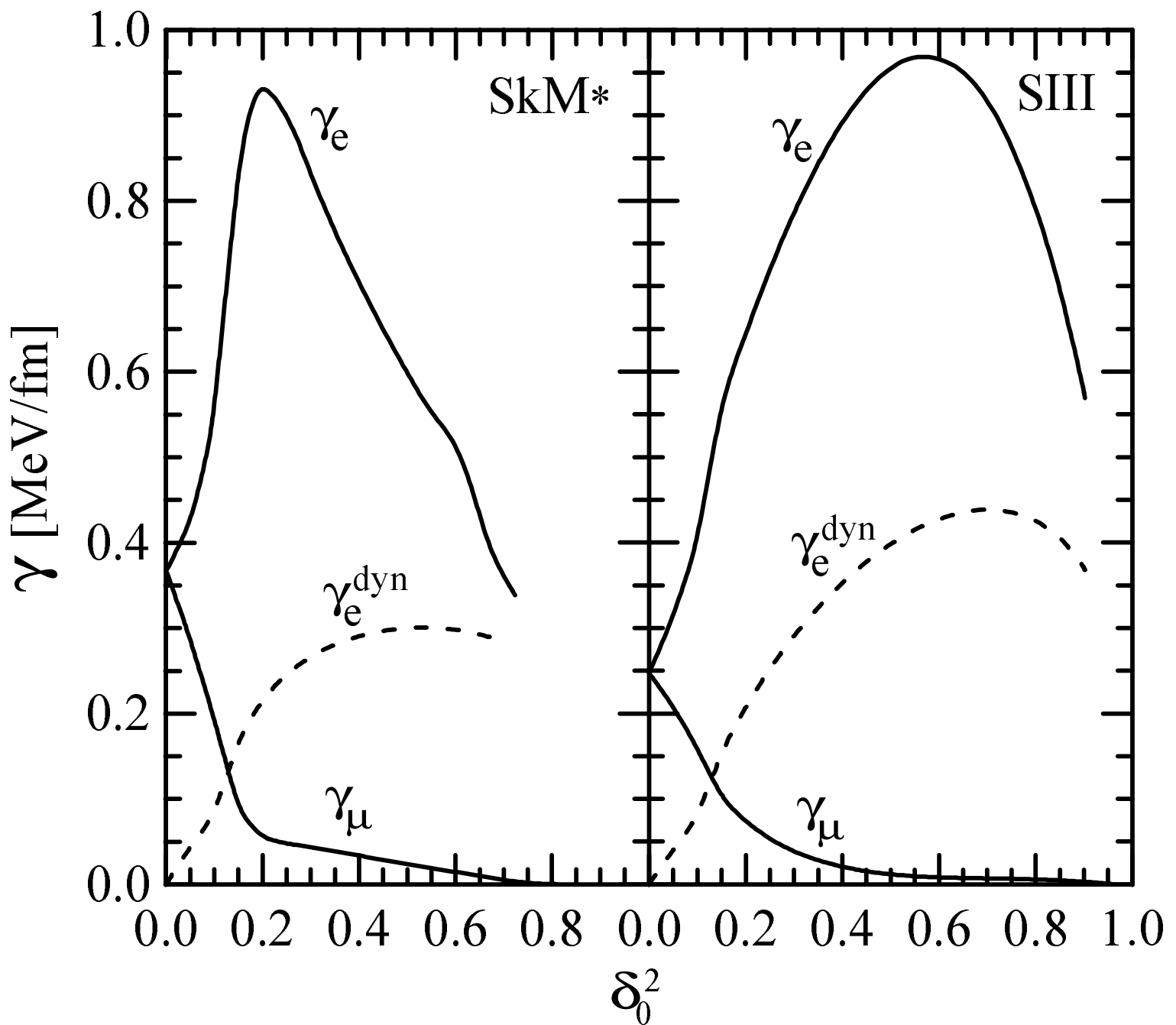
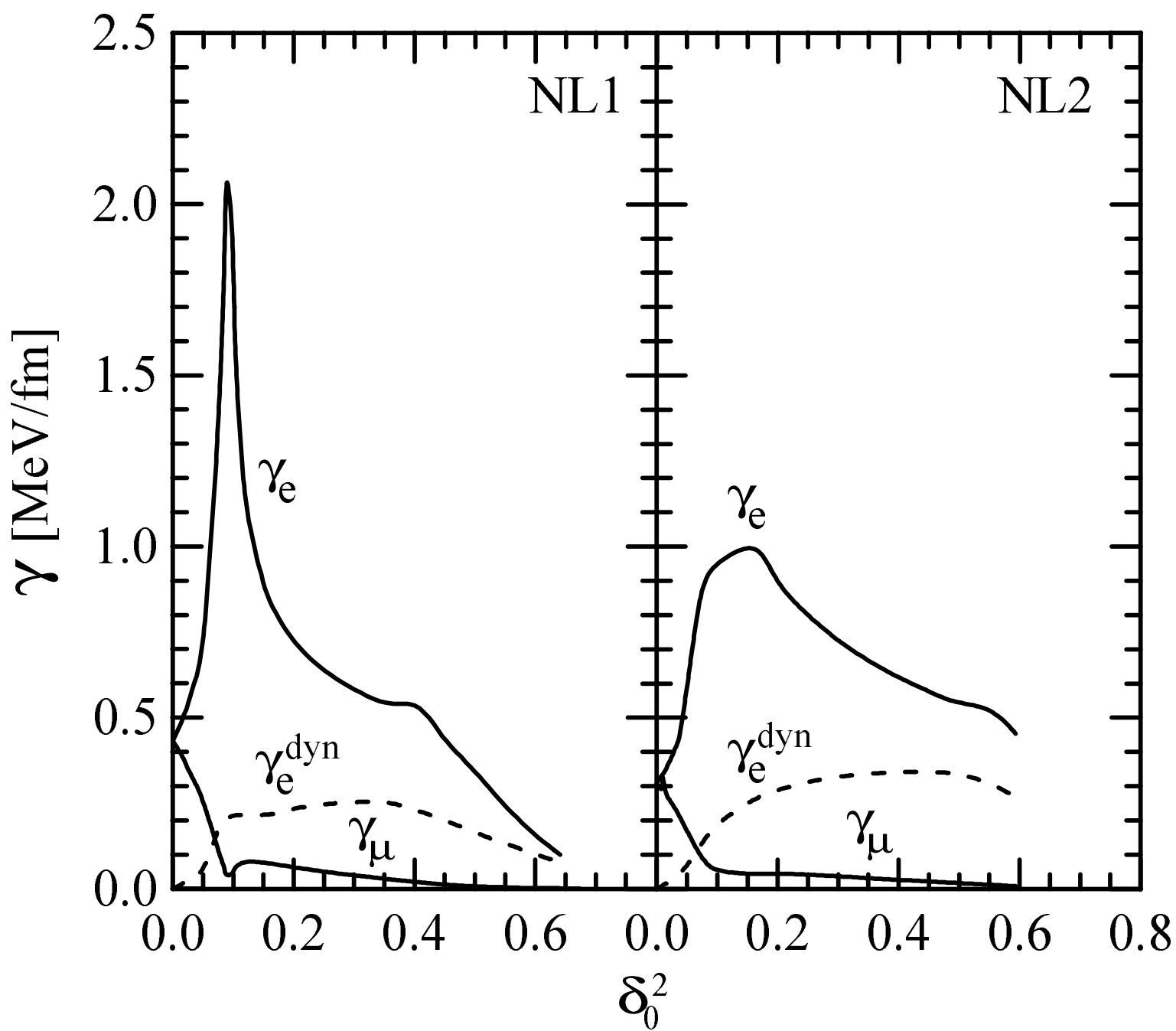


Figure 14



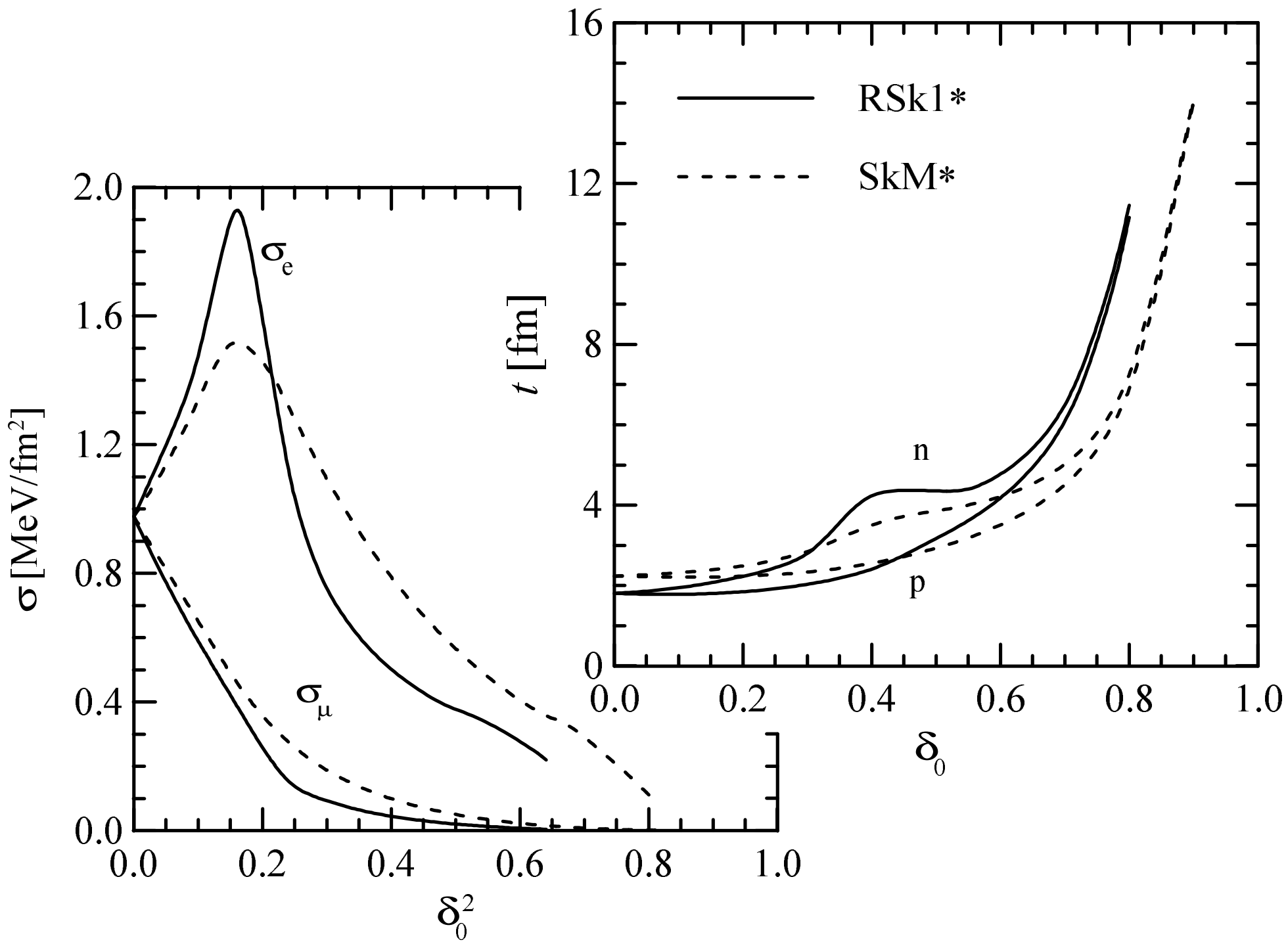


Figure 16

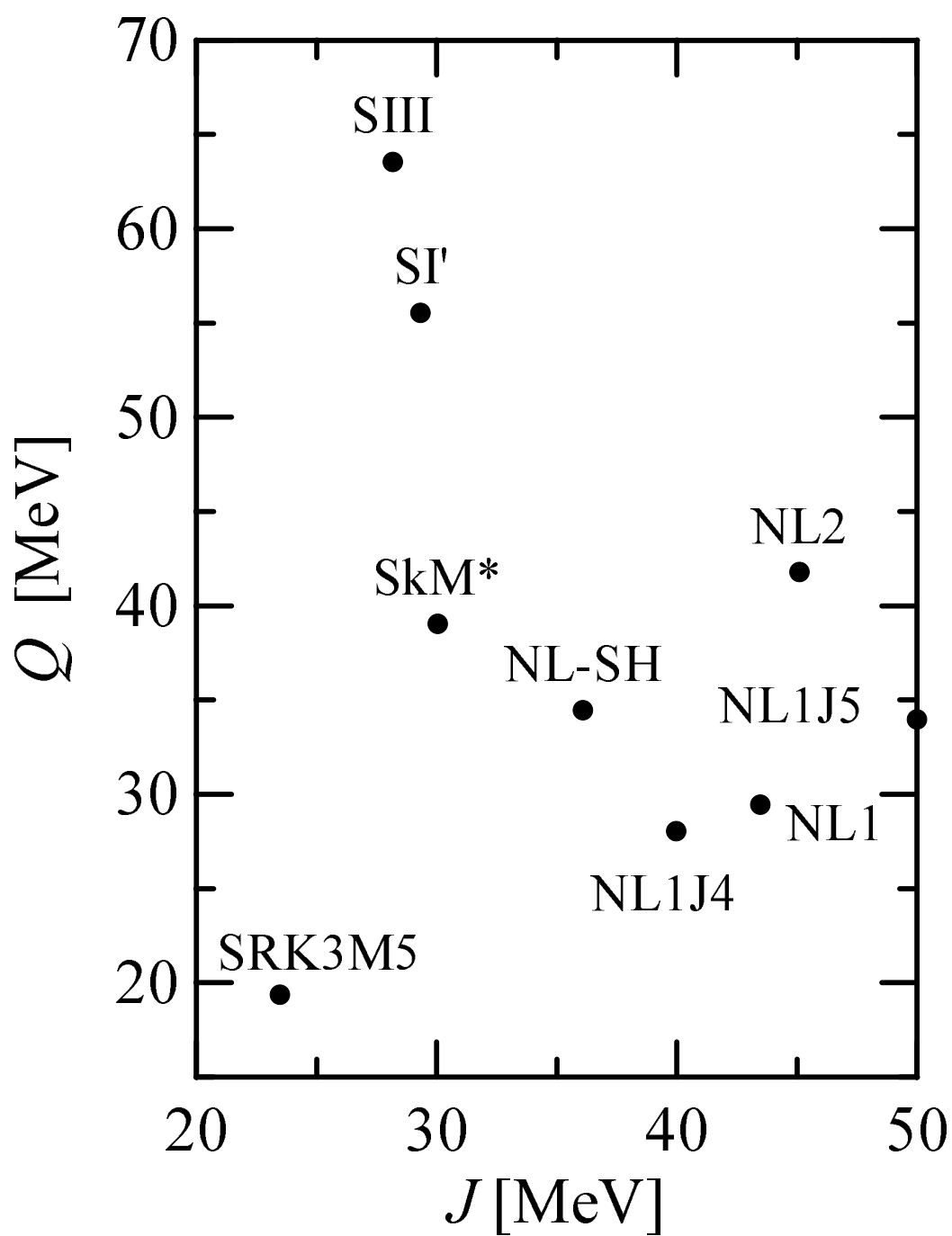


Figure 17

